

# 1 **Single-particle Raman Spectroscopy for studying** 2 **physical and chemical processes of atmospheric particles**

3 Zhancong Liang<sup>1</sup>, Yangxi Chu<sup>2</sup>, Masao Gen<sup>3</sup>, Chak K. Chan<sup>1\*</sup>

4 <sup>1</sup> School of Energy and Environment, City University of Hong Kong, Hong Kong, 999077, China.

5 <sup>2</sup> State Key Laboratory of Environmental Criteria and Risk Assessment, Chinese Research Academy of  
6 Environmental Sciences, Beijing, 100012, China.

7 <sup>3</sup> Faculty of Frontier Engineering, Institute of Science and Engineering, Kanazawa University,  
8 Kanazawa, 920-1192, Japan.

9 *Correspondence to:* Chak K. Chan ([chak.k.chan@cityu.edu.hk](mailto:chak.k.chan@cityu.edu.hk))

10  
11 **Abstract.** Atmospheric particles experience various physical and chemical processes and change their  
12 properties during their lifetime. Most studies on atmospheric particles, both in laboratory and field  
13 measurements, rely on analyzing an ensemble of particles. Because of different mixing states of  
14 individual particles, only average properties can be obtained from studies using ensembles of particles.  
15 To better understand the fate and environmental impacts of atmospheric particles, investigations on their  
16 properties and processes at a single-particle level are valuable. Among a wealth of analytic techniques,  
17 single-particle Raman spectroscopy provides an unambiguous characterization of individual particles  
18 under atmospheric pressure in a non-destructive and in-situ manner. This paper comprehensively reviews  
19 the application of such a technique in the studies of atmospheric particles, including particle  
20 hygroscopicity, phase transition and separation, and solute-water interactions, particle pH, and  
21 multiphase reactions. Investigations on enhanced Raman spectroscopy and bioaerosols on a single-  
22 particle basis are also reviewed. For each application, we describe the principle and representative  
23 examples of studies. Finally, we present our views on future directions on both technique development  
24 and further applications of single-particle Raman spectroscopy in studying atmospheric particles.

## 32 **1 Background**

33 Atmospheric particles or aerosols have considerable effects on climate and human health (Seinfeld and  
34 Pandis, 2016). In general, atmospheric particles can originate from a wide variety of anthropogenic and  
35 natural sources. Primary particles are emitted directly as a liquid or solid (e.g., soot particles, mineral  
36 dust), and they can also undergo atmospheric multiphase reactions. Secondary particles can also be  
37 generated by gas-to-particle conversions, such as new particle formation via nucleation and condensation  
38 (Pöschl, 2005). During their atmospheric lifetime, both primary and secondary particles are subject to  
39 physical and chemical processes, such as partitioning and multiphase reactions. For liquid particles, gas-  
40 particle partitioning takes place to achieve thermodynamic equilibrium. For example, an increase or  
41 decrease in relative humidity (RH) would result in the uptake of the water vapor into deliquescent  
42 particles or the evaporation of particulate water to the gas phase, respectively. Multiphase reactions can  
43 be described as gas-particle partitioning accompanied by chemical reactions. Furthermore,  
44 photochemistry is an important group of multiphase reactions during the daytime. Both partitioning and  
45 chemical reactions can change the composition of the particles, altering their properties such as  
46 hygroscopicity, cloud condensation nuclei (CCN) activities, phase state, morphology, reactivity, toxicity,  
47 and finally, environmental impacts.

48

49 Physical and chemical processes of atmospheric particles have been examined by numerous experimental  
50 approaches: a flowing stream of aerosol particles in an open system (flow tube) (Li et al., 2015; Duporté  
51 et al., 2017; Heine et al., 2018; Liu and Abbatt, 2020; Liu et al., 2020a; Peng and Jimenez, 2020), a chamber  
52 of suspending particles (smog chamber) (Akimoto et al., 1979; Behnke et al., 1988; Liu et al., 2016; Ye et  
53 al., 2018; Charan et al., 2019; Liu and Abbatt, 2021; Qin et al., 2021), a collection of deposited particles  
54 (Bao et al., 2018; Zhang et al., 2020b), and single particles (Lee and Chan, 2007a; Krieger et al.,  
55 2012; Davies and Wilson, 2016; Gen et al., 2019b; Gong et al., 2019; Sullivan et al., 2020). An aerosol flow  
56 tube is one of the most common approaches employing a flowing stream of aerosol particles. It enables  
57 real-time characterization of reaction products and particulate size under controlled conditions (e.g., RH,  
58 temperature), with instruments connected to the exit or different outlets along the flow tube reactor.  
59 Oxidation flow reactors (OFR) are analogous to the general aerosol flow tube, but photooxidants (e.g.,  
60 OH radical) are introduced to examine secondary organic matter formation (Kang et al., 2007; Smith et  
61 al., 2009; George and Abbatt, 2010; Keller and Burtscher, 2012). Typically, higher concentrations of

62 reactive precursor gases than ambient concentrations are used in these flow systems to compensate for  
63 the relatively short residential time (e.g., seconds) of the reactants. However, such equivalency of  
64 exposure may not necessarily hold (Lee and Chan, 2007b; Chu et al., 2019). Smog chambers enable  
65 simulations of various environmental conditions, including gas concentrations, for studying the  
66 formation and chemical transformation of particles. The residence time of particles can be extended to a  
67 few hours, but other limitations exist, such as long response time to control/change conditions, high cost,  
68 and wall loss of particles (Kang et al., 2007). Deposited particles can be studied using a sample-loaded  
69 substrate/filter placed in a flowing-gas reactor or a flow tube with its internal wall coated with particles.  
70 Environmental conditions can be easily varied, and the reaction time can be very long. An in-situ analyzer  
71 for spectroscopic analysis can be equipped (e.g., Raman, Fourier Transform Infrared Spectrometry (FT-  
72 IR)) since the particles are immobilized on a substrate/filter. However, using a large number of particles  
73 or large particles is usually required to achieve sensitive detection. The influence of particle loading on  
74 the reactions and chemical characterization is a challenging question. In general, these approaches  
75 produce statistical results of a collection of particles. They may not truly reflect the interaction between  
76 gas and particle since the composition of the individual particles may not be identical (Ault and Axson,  
77 2017).

78

79 Single-particle characterization has the advantage that the physical and chemical processes undertaken  
80 by the particle can be unambiguously monitored. While there is a wealth of instruments for  
81 comprehensively characterizing single particles, some are destructive (e.g., mass spectroscopy) or  
82 operate under vacuum conditions (e.g., electron microscopy), making them unsuitable for monitoring the  
83 gas-particle interaction on the same particles. Single-particle spectroscopic methods (e.g., Raman) can  
84 be good alternatives, but the particles are usually supermicron and up to tens of microns. The findings  
85 from particles much larger than ambient ones need to be interpreted carefully for drawing implications  
86 in submicron atmospheric particles.

87

88 Despite its requirements of relatively large particles for spectroscopic signals, single-particle Raman  
89 spectroscopy offers several advantages for studying the atmospheric [processing](#) of aerosol particles. First  
90 of all, a single particle can be unambiguously characterized *in situ* without destruction. From the Raman  
91 spectra, chemical compositions of typical aerosol particles (e.g., soot, sulfate, organics, etc.) can be

92 identified by their characteristic peaks. Interactions between molecules can be inferred by peak shifts  
93 and changes in peak width. Particulate properties such as the phase state and size can also be  
94 characterized by coupling levitation (or isolation) technique and optical microscopy. We will elaborate  
95 on the applications of these functions later.

96  
97 Furthermore, Raman analysis is operated under atmospheric pressure and enables the use of atmospheric  
98 relevant concentrations for a long exposure time to examine atmospheric gas-particle interactions (Lee  
99 and Chan, 2007a). Micro-Raman systems provide the spatial information of chemical species at 2-D or  
100 even 3-D levels (Batonneau et al., 2006;Sobanska et al., 2006;Tripathi et al., 2009;Scolaro et al.,  
101 2009;Sobanska et al., 2014;Offroy et al., 2015;Sobanska et al., 2015;Falgayrac et al., 2018;Ao et al.,  
102 2020). Recent advances in stimulated Raman scattering by micro-Raman further improves the spatial  
103 resolution from 1  $\mu\text{m}$  to 350 nm and significantly shortens the scanning time from 2.5 h to 2 s (Ao et al.,  
104 2020). The disadvantage of Raman spectroscopy is that it can only detect Raman-active functional groups  
105 but cannot provide information on the exact molecular structures. Light-absorbing chemicals such as  
106 [humic-like substances](#) (HULIS) or some brown carbon species may generate fluorescence, interfering  
107 with the peak identification in the spectra (Ivleva et al., 2007a). Therefore, single-particle Raman  
108 spectroscopy is more suited for laboratory-generated particles than ambient particles. FTIR does not  
109 suffer from fluorescence since it uses a longer wavelength (up to tens of  $\mu\text{m}$ ), but the long wavelength  
110 also lowers the spectral resolution (Ault and Axson, 2017;Liu et al., 2020b). Also, Raman has advantages  
111 over FTIR for water-containing samples because the strong water peaks in the latter can mask the peaks  
112 from other components or even make them undetectable (Nishikida et al., 2018).

113  
114 This paper will introduce the general setup of the single-particle Raman spectrometer, how single  
115 particles can be characterized unambiguously, and examples of physical and chemical processes reported  
116 in the literature. We focus on applications of atmospheric relevance and refer readers to other literature  
117 on the principles of Raman spectroscopy and related techniques (e.g., stimulated Raman or coherent  
118 Anti-stokes Raman spectroscopy) and applications of less direct atmospheric relevance (Tolles et al.,  
119 1977;Efremov et al., 2008;Jones et al., 2019). Finally, we will provide suggestions on future directions  
120 of Raman spectroscopy for atmospheric particle studies.

121

## 122 **2 General set up of single-particle Raman spectroscopy**

### 123 **2.1 Particle isolation**

124 In general, single-particle Raman spectroscopy consists of two key components: particle isolation and  
125 Raman spectroscopy, including micro-Raman and confocal Raman configurations. One of the most  
126 popular approaches for single-particle isolation is particle levitation, which has been discussed in a few  
127 reviews (Reid and Mitchem, 2006; Mitchem and Reid, 2008; Krieger et al., 2012). In this paper, we will  
128 briefly introduce their principles and configurations and focus on atmospheric applications. Techniques  
129 for levitation of particles can be mainly divided into electrical, optical, and acoustic trapping. Another  
130 approach for particle isolation is particle deposition onto substrates with Raman analyses of single  
131 particles on an individual basis.

132

#### 133 **2.1.1 Electrodynamic balance**

134 The Electrodynamic balance (EDB) has been used for studying single particles with a diameter of 1-  
135 100 $\mu\text{m}$  since the 1980s (Davis and Ray, 1980). A particle is levitated and trapped at the null point under  
136 the alternating current (AC) and direct current (DC) electric fields in the EDB. In the absence of other  
137 forces, the gravitational force of the particle trapped in the EDB is equal to the balancing electrostatic  
138 force, as shown in Eq. (1)

$$139 \quad mg = nqC \frac{V_{DC}}{z} \quad (1)$$

140 where  $m$  is the mass of the particle,  $g$  is the gravitational constant,  $n$  is the number of elementary  
141 charges present on the particle,  $q$  is the elementary charge,  $z$  is the distance between two electrodes  
142 for the DC voltage,  $C$  is a constant dependent on the geometrical configuration of the EDB, and  $V_{DC}$   
143 is the balancing DC voltage required to levitate the particle stationary. According to Eq. (1), the mass of  
144 the particle is proportional to the DC voltage needed to balance its gravitational force, assuming that the  
145 charge present on the trapped particle remains constant. Hence, the relative mass change in the particle  
146 undergoing any physical or chemical processing can be quantified by measuring the balancing DC  
147 voltage. With a particle levitated stationary, Raman spectroscopy of the stably trapped particles can  
148 provide chemical information. Coupled with mass change measurements and optical microscopy,  
149 physical and chemical characterization of single particles can be in-situ monitored. In addition to the  
150 traditional single-particle EDB (Davis and Ray, 1980; Chan et al., 1992), other EDB set-ups, for

151 example, quadrupole (Q)-EDB and comparative kinetic (CK)-EDB, have been developed. Q-EDB  
152 allows the trapping of multiple droplets simultaneously. During chemical reactions, individual  
153 particles are released one at a time for mass spectroscopy analysis while the rest of the particles are  
154 kept levitated for in-situ spectroscopic characterization (Singh et al., 2017; Jacobs et al., 2017; Singh  
155 et al., 2018; Kohli and Davies, 2021). CK-EDB employs a reference droplet with known composition  
156 and hygroscopic property, which serves as an accurate probe for the environmental conditions in  
157 which the tested droplet is examined. It affords hygroscopicity measurements and mass-transfer  
158 kinetic measurements on the droplets at high RH (>99%) (Davies et al., 2013; Rovelli et al.,  
159 2016; Marsh et al., 2019).

160

### 161 **2.1.2 Optical trapping**

162 Optically traps can be basically categories into radiation pressure trap, photophoretic trap and universal  
163 optical trap. Radiation pressure trap, which is the most general in studying aerosol particles, utilizes the  
164 radiation pressure from a light source to balance the weight of the levitated particle (Ashkin, 1970).  
165 During optical trapping, the particle interacts with a highly focused laser beam and experiences scattering  
166 and gradient forces (Ashkin and Dziedzic, 1981; Mitchem and Reid, 2008). The scattering force is  
167 proportional to the square of the induced dipoles and the intensity of the incident laser beam, acting as a  
168 force along the direction of the beam propagation. In contrast, the gradient force derives from the  
169 focusing of the laser beam and draws the particle towards the region with the highest light intensity  
170 (Krieger et al., 2012).

171

172 Radiation pressure-based optical levitation and optical tweezer are two typical optical-trapping  
173 techniques utilizing these two forces. While optical levitation relies on the exact balance between  
174 downward gravitational force and upward scattering force, optical tweezers effectively create a strong  
175 intensity gradient in three dimensions by tightening the focus of the laser beam to generate amplified  
176 gradient forces. Optical tweezers provide a more robust trap with the gradient force typically many orders  
177 of magnitude larger than the scattering and gravitational forces, leading to 3-dimensional confinement in  
178 position with a single laser beam. However, particle size changes must be accompanied by dynamic  
179 changes in the light intensity for retaining the trapped particle. In principle, transparent non-absorbing  
180 particles of 1–100  $\mu\text{m}$  in diameter can be trapped with dynamic light intensity adjustment for droplet size

181 changes. By configuring a Bessel laser beam, instead of the typical Gaussian beam, in either vertically  
182 or horizontally trapping arrangements, optical levitation and tweezer can be applied for trapping  
183 submicron particles (Meresman et al., 2009;Cotterell et al., 2014;Lu et al., 2014). However, Raman  
184 spectroscopy would require larger particles for sufficient signal-to-noise ratios. A recent study reported  
185 a photochemical study of aerosol particles using an optical trap for the first time by employing a custom-  
186 built photochemical levitation chamber (Gómez Castaño et al., 2019). A sidewall of the chamber is  
187 equipped with quartz windows for a UV lamp.

188

189 In addition to radiation pressure traps, photophoretic traps and universal optical traps are two emerging  
190 alternatives (Redding et al., 2015a;Redding and Pan, 2015). The former is specifically for light-absorbing  
191 particles. The latter employs a hollow beam to trap either transparent and light-absorbing particles using  
192 radiation pressure force and photophoretic force, respectively (Gong et al., 2018a). Using these  
193 techniques, Raman characterizations have been made on light-absorbing particles in recent years,  
194 including bioaerosols (Wang et al., 2015a;Redding et al., 2015a;Redding et al., 2015b;Gong et al., 2018b,  
195 2019), aromatic compounds (Kalume et al., 2017b;Kalume et al., 2017a;Gong et al., 2018b), carbon  
196 nano-tubes (Pan et al., 2012;Gong et al., 2018b) and soot (Uraoka et al., 2017).

197

### 198 **2.1.3 Acoustic levitation**

199 Compared to the EDB and optical trap, acoustic levitation is less utilized in atmospheric research due to  
200 the complicated acoustic streaming and the requirement for large particles (20  $\mu\text{m}$ - 2 mm.) (Cohen et al.,  
201 2020;Jones et al., 2021). In an acoustic levitator, high-frequency sound waves generated by a piezo-  
202 electric radiator reflect from a concave-shaped reflector to generate a standing wave. The latter produces  
203 acoustic radiation pressure on the particle, levitating and trapping it against the gravitational force. It has  
204 been reported that a single particle can be firmly trapped by acoustic levitation under 15 h continuous  
205 irradiation (Tobon et al., 2017;Seng et al., 2018).

206

### 207 **2.1.4 Deposited particles**

208 In addition to single-particle levitation, deposited particles on a surface provide a convenient platform  
209 for single-particle Raman spectroscopy. While levitation can trap few particles for investigation, surface-  
210 based isolation affords a relatively large number of single particles, which can support further off-line

211 characterizations. However, the direct contact between particle and substrate may induce solute  
212 nucleation or phase separation that causes unexpected modification in particulate morphology. Hence,  
213 hydrophobic substrates are often used to study supersaturated aqueous droplets by reducing the particle  
214 and substrate contact area. Investigations on photochemistry can be easily performed by coupling a  
215 transparent substrate and an additional light source beneath the quartz window at a flow cell's bottom  
216 (Gen et al., 2019b; Gen et al., 2020). A single particle can be retained for an infinite time deposited,  
217 facilitating studies of slow processes in the atmosphere. However, Raman scattering from the substrate  
218 could also show interference.

219

## 220 **2.2 Raman spectroscopy**

221 A single particle Raman spectroscopy set-up generally involves a laser for excitation, followed by  
222 collection optics to detect the Raman signals analyzed by a spectrometer with a monochromator and a  
223 CCD detector. The Raman peak location and intensity/area provide information on the speciation and  
224 abundance of specific particulate components. Appendix A summarizes the Raman peak assignment of  
225 representative atmospheric species. Raman peak can also shift its location (in wavenumber) and change  
226 in the full width at half-maxima (FWHM) as a response to variations of local bonding environments,  
227 such as molecular interaction and phase transition. Furthermore, Raman emissions from spherical  
228 particles (e.g., levitated droplets) can be complicated by resonance modes at discrete wavelengths  
229 triggered by cavity-enhanced Raman scattering (CERS) (Miles et al., 2012), or so-called size parameters  
230 in the spectra. These resonant modes are often called morphology-dependent resonance (MDRs) or  
231 whispering gallery modes (WGMs) (Chan et al., 1991; Krieger et al., 2012). They can accurately  
232 determine size with a resolution down to ~5 nm, refractive index, and even shell-core morphology of the  
233 mixed organic-inorganic particles based on the Mie theory (Gorkowski et al., 2017; Rafferty and Preston,  
234 2018; Sullivan et al., 2020; Gorkowski et al., 2020). The optical effects complicate the Raman  
235 measurements for chemical analysis, although they provide additional information for the sizing and  
236 refractive index of the particles based on Mie theory. We refer readers to the references for the  
237 interactions between Mie scattering and Raman spectroscopy (Chan et al., 1991; Krieger et al.,  
238 2012; Nadler et al., 2019). Micro-Raman is a combined system that uses an optical microscope for guiding  
239 the laser to analyte particles and collect Raman scattering from the same microscope connected to a  
240 spectrometer. The Raman scattering signal-to-noise ratio can be enhanced since the incident laser energy



241 is focused on a small volume through a high magnification (and short working distance) objective.  
242 Furthermore, 2D Raman imaging is possible in studying particles in the order of tens of microns (Eom  
243 et al., 2016;Zhao et al., 2018). Confocal Raman micro-spectroscopy eliminates the Raman scattering  
244 from volumes other than the focal volume by configuring additional slits in the spectrometer. Confocal  
245 Raman provides depth profiles of constituent information of the particle (Scolaro et al., 2009).

246

247 This paper focuses on the use of single-particle Raman spectroscopy to examine the physical and  
248 chemical processes of atmospheric particles. We describe techniques of particle maneuvering that allow  
249 single-particle Raman spectroscopy such as EDB, deposited particles, and optical trapping. However, it  
250 is not our intention to conduct a detailed examination of the application of these techniques beyond  
251 single-particle Raman spectroscopy. Hence, in this review, we put less emphasis on literature related to  
252 other applications of these trapping techniques. We focus on investigating these physical and chemical  
253 processes of particles by Raman instead of the particle properties or detailed descriptions of these  
254 processes investigated by other techniques. The overall aim of the paper is to introduce single-particle  
255 Raman spectroscopy as a useful tool to examine a host of processes of atmospheric relevance.

256

### 257 **3 Characterization of single particles**

#### 258 **3.1 Hygroscopicity and phase transition**

259 Depending on the environmental RH, type of solutes, and size of the particles (Kelvin effect),  
260 atmospheric particles can absorb/release an appropriate amount of water to reach equilibrium with the  
261 gas phase, i.e., the partial water vapor pressure above the particle surface equals to that of the gas phase.  
262 Hygroscopic properties include water uptake/evaporation and phase transition as a response to changes  
263 in ambient RH. Upon water uptake/evaporation, the particle size change alters the particulate capacity in  
264 scattering light, and particles can also be activated to cloud condensation nuclei (Tang et al., 2019). In  
265 this paper, we focus on subsaturated ( $RH < 100\%$ ) environments. The phase states determine the water  
266 uptake behaviors of the atmospheric particles (Pajunoja et al., 2016;Rosati et al., 2020). They can be  
267 generally divided into liquid (i.e., aqueous), crystalline, and amorphous (e.g., ultra-viscous, gel, rubber,  
268 glasses). Both crystalline and amorphous particles are solids, but only the latter can absorb water  
269 reversibly, while the former shows hysteresis in water uptake. At increasing RH, water uptake increases  
270 the aerosol liquid water (ALW) content of deliquescent/amorphous particles and their size and ability to

271 scatter light. A recent study showed that the poor visibility during haze in the North China Plain is  
272 positively correlated to the ALW(Wu et al., 2018b). When crystalline particles are exposed to increasing  
273 RH, they will initially adsorb a small amount of water on its surface, the so-called surface adsorbed water  
274 (SAW), and then uptake a significant amount of water vapor abruptly to become aqueous droplets at the  
275 deliquescence RH (DRH). The DRH is the RH at which a droplet attains the saturated salt concentration,  
276 ignoring the influence of the Kelvin effect, which is often the case for single-particle Raman analysis  
277 (particle size > 10  $\mu\text{m}$ ). At decreasing RH, a droplet loses water to become supersaturated and finally  
278 may effloresce to form crystalline particles at the efflorescence RH (ERH). Typical inorganic  
279 atmospheric components of  $(\text{NH}_4)_2\text{SO}_4$ ,  $\text{NH}_4\text{NO}_3$  and NaCl deliquesce at ~80%, ~62% and ~75% RH  
280 but effloresce at 34-48%, 0-30% and 39-54%, respectively. Many studies show that nitrates and some  
281 organics do not effloresce even at low RH (e.g., below 5%) (Mikhailov et al., 2009;Yeung and Chan,  
282 2010). In general, organics with high solubility (e.g., malonic acid) tend to remain a supersaturated liquid  
283 state or amorphous state at low RH (Krieger et al., 2012). Unlike DRH, which is thermodynamically well  
284 defined, ERH is a stochastic property that relates to the kinetics of nucleation and presence of impurities.  
285 It has been reported that sucrose crystals deliquesce at 85.6%RH upon humidification, but the aqueous  
286 droplets turn into a glassy amorphous state upon drying instead of forming crystallized solids (Zobrist et  
287 al., 2011). Using EDB and optical trap experiments, hygroscopic changes and phase transition RH values  
288 that involve rapid changes in mass or size can be measured by the balancing voltage and light scattering,  
289 respectively. The growth factor (GF) in terms of mass or size ratios as a function of water activity or RH,  
290 DRH, and ERH can be easily determined by changes in mass/size and the light scattering pattern (Chan  
291 et al., 2005;Mitchem et al., 2006;Marsh et al., 2017).

292

293 While GF, DRH, and ERH measurements are readily made for mixed particles using EDB and optical  
294 traps, the formation of mixed-phase particles before full deliquescence is more complicated. For example,  
295 unlike the corresponding single inorganic salts, NaCl-malonic acid and  $(\text{NH}_4)_2\text{SO}_4$ -malonic acid mixed  
296 particles absorb a significant amount of water before their DRH since malonic acid absorbs water  
297 reversibly without crystallization (Lee et al., 2008a). However, this stepwise water uptake and phase  
298 transition behaviors could not be explained by EDB/optical levitation due to the lack of chemical  
299 characterization. Raman spectroscopy offers complementary information on the water uptake behaviors  
300 and phase states of Raman active species (Yeung and Chan, 2010;Li et al., 2017). For example, the water-

301 to- solute ratio (WSR) as a function of ambient RH can be easily determined from the integrated peak  
302 area ratio of the water  $\nu(\text{O-H})$  to that of the solute (e.g., sulfate, nitrate) after proper calibration. Also,  
303 the full width at half maxima (FWHM) of the characteristic peaks is sensitive to the phase state of the  
304 solute. In general, a species in the liquid phase has a larger FWHM than in the solid phase because the  
305 less compact molecular arrangement allows minor variations in vibration. In Fig. 1a,b, as the RH  
306 decreased to 39.5% for ammonium sulfate (AS) and 19% for ammonium nitrate (AN), crystallization  
307 can be inferred by the red-shift and decrease in FWHM of sulfate and nitrate peaks, and the disappearance  
308 of water peak. On this basis, the mixed-phase particle prior to full deliquescence can be characterized by  
309 FWHM of different Raman-active components. For instance, Ling and Chan found an increased FWHM  
310 of nitrate peak ( $\sim 730 \text{ cm}^{-1}$ ) at  $\sim 67\%$  RH, followed by an increased FWHM of sulfate peak ( $\sim 450 \text{ cm}^{-1}$ )  
311 at  $\sim 76 \text{ RH}\%$  for mixed-phase AS-AN particles when RH increased (Fig. 1c,d). These changes indicate  
312 that AN deliquesced before AS did upon humidification, and the mixed-phase AS-AN particle was  
313 composed mainly of aqueous AN and crystalline AS. The accuracy of single-particle Raman  
314 spectroscopy in determining hygroscopicity has been verified by thermodynamic models such as E-AIM  
315 and UNIFAC (Peng et al., 2001; Yeung and Chan, 2010). There are numerous hygroscopicity applications  
316 on various specific systems, including model inorganics, organics, and their mixtures (Chu et al.,  
317 2015; Laskina et al., 2015; Wang et al., 2021b; Tobon et al., 2021; Zhang et al., 2021a; Ashraf et al., 2021)  
318 mineral dust (Liu et al., 2008), secondary organic aerosols (Wu et al., 2020), atmospheric-relevant  
319 biological macromolecules (Mael et al., 2021) using single particle Raman spectroscopy. It should be  
320 noted that evaporation of some components and precipitation of some salts could occur during the  
321 RH cycling in hygroscopicity measurements (Li et al., 2017; Cai and Zhao, 2018; Ma et al., 2019a; Ma  
322 et al., 2019b; Wu et al., 2020; Li et al., 2021). Single-particle Raman spectroscopy can probe such  
323 processes in-situ by the disappearance of some characteristic peaks (evaporation) or changes of their  
324 FWHH (precipitation) (Braban et al., 2003; Wang et al., 2017).

325

### 326 **3.2 Solid-phase transition**

327 In addition to liquid-solid phase changes, transitions can occur between solid phases, from a metastable  
328 one to a stable one at a specific temperature. Many organics are known to form polymorphs, defined as  
329 solids with the same chemical composition but distinctive properties such as thermal stability and  
330 solubility due to different structures (Krieger et al., 2012). Different polymorphs of the same compound

331 can exhibit different Raman characteristics, which can identify different solid states and their transition.  
332 For example, crystalline glutaric acid (GA) particles could exist as the metastable  $\alpha$ -form and the  
333 thermodynamically stable  $\beta$ -form at room temperature, and  $\alpha$ -form GA tends to transfer into  $\beta$ -form.  
334 Using EDB-Raman, Chan et al. (2006) coated GA on AS particles by coagulation of small GA particles  
335 formed by nucleation. Raman spectra showed the existence of  $\alpha$ -form GA in the freshly coated particles,  
336 but then  $\beta$ -form was detected after a deliquescence - crystallization cycle (Chan et al., 2006). Ling and  
337 Chan (2008) reported the formation of the  $\alpha$ -form GA solid in a freshly crystallized GA-AS particle.  
338 The  $\alpha$ -form GA solid gradually transformed to the  $\beta$ -form at 60% RH in 3 h at room temperature (Ling  
339 and Chan, 2008). Furthermore, Yeung et al. (2010) examined the effects of polymorphism on the  
340 hygroscopic properties of GA particles using Micro-Raman (Yeung et al., 2010). By evaporation at room  
341 temperature,  $\alpha$ -form and  $\beta$ -form solid particles were formed ( $\alpha:\beta \approx 5:1$ ). It was observed that the  $\alpha$ -  
342 form deliquesced at 85-86% RH, whereas the  $\beta$ -form deliquesced at 90% RH. Furthermore, the  $\alpha$ -form  
343 is transformed to the  $\beta$ -form at 86% RH instead of achieving full deliquescence (Fig. 2). This solid  
344 phase transition behavior was used to explain the discrepancies of DRH values of glutaric acid particles  
345 reported based on different literature measurements (Cruz and Pandis, 2000; Peng et al., 2001; Choi and  
346 Chan, 2002; Parsons et al., 2004; Zardini et al., 2008; Treuel et al., 2009). Polymorphism also exists in  
347 atmospheric relevant inorganics. For example, AN can exist in five stable polymorphic forms with  
348 distinct Raman spectra, depending on the temperature. In atmospheric research, very little attention has  
349 been paid to the solid phase transitions of AN because phase IV AN particle is stable over a wide range  
350 of tropospheric temperatures ( $-17^{\circ}\text{C}\sim 32^{\circ}\text{C}$ ) (Wu et al., 2007). Nevertheless, Wu and Chan (2008)  
351 reported that the  $\text{KNO}_3/\text{AN}$  mixed particles undergo the IV-III transition under ambient temperatures at  
352 a relatively high mass percentage of  $\text{KNO}_3(\geq 7.4 \text{ wt}\%)$ , or even crystallize directly in phase III from  
353 droplets with a further increase in the mass percentage of  $\text{KNO}_3$  (Wu and Chan, 2008).

354

355 Another typical solid phase transition is between stable/metastable double salts. Like metastable/stable  
356 polymorphs, metastable double salts show Raman characteristics different from stable ones, likely due  
357 to specific molecular interactions. Ling et al. (2007) observed the double-salt  $3\text{AN}\cdot\text{AS}$ , not predicted  
358 from thermodynamics, in the freshly crystallized mixed single particles of AN and AS using single-  
359 particle Raman spectroscopy (Ling and Chan, 2007). The existence of double salts indicates that AN and  
360 AS likely crystallized simultaneously. The degree of metastability could depend upon the crystallization

361 processes of the particles. Besides, it takes several hours to more than a day, depending on RH, for a  
362 freshly crystallized metastable AS-AN double salt particle to reach its stable form, suggesting a high  
363 possibility that metastable solids persist in the atmosphere when the ambient RH is sufficiently low. The  
364 AN-AS double salts were recently reported in ambient particles in Beijing (Sun et al., 2019b; Wang et al.,  
365 2021a).

366

### 367 **3.3 Molecular interactions between particulate water and solutes**

368 In general, characterizations on phase transitions relies on the sensitivity of Raman spectroscopy in  
369 probing the bonding environment of components in the particles. Raman can also characterize the  
370 interactions between the solutes and particulate water, such as hydrogen/ionic bonding. For example, the  
371 Raman shift of strongly hydrogen-bonded water ( $\sim 3500\text{ cm}^{-1}$ ) is generally higher than that of water  
372 monomers ( $\sim 3300\text{ cm}^{-1}$ ) (Zhang and Chan, 2003). At low RH, the elevated concentration of electrolytes  
373 leads to more significant disruption of the hydrogen bonding environment of the water molecules,  
374 resulting in a shift of OH stretching peak at  $3480\text{ cm}^{-1}$  to higher frequencies. In contrast, the low-  
375 frequency shoulder at  $3290\text{ cm}^{-1}$  diminishes. Thus, the shape of water peaks in Raman spectra can reflect  
376 the ionic strength of the particle, which is an essential parameter for aerosol chemistry (Mitchem et al.,  
377 2006; Mekic et al., 2020). The sensitive shift of water peak has also been used in studying ice nucleation  
378 properties such as depositional freezing (Wise et al., 2010; Wise et al., 2012) and immersing freezing  
379 (Knopf et al., 2002; Knopf et al., 2003). Specifically, while liquid water peaks are usually located at  
380  $\sim 3400\text{ cm}^{-1}$  with a shoulder at a lower wavenumber, a sharp peak at  $\sim 3150\text{ cm}^{-1}$  with shoulder peaks at  
381  $\sim 3200\text{ cm}^{-1}$  appears as water is frozen (Schill et al., 2014; Mael et al., 2019). Besides, ionic bonding of  
382 inorganic salts (e.g.,  $\text{SO}_4^{2-}$ ,  $\text{NO}_3^-$ ) can also be reflected by their Raman characteristics; and many of them  
383 have been further supported by theoretical calculations (Yu et al., 2012; Wang et al., 2015b; Zhu et al.,  
384 2018). For example, Zhang et al. observed a blue shift of sulfate and nitrate Raman peaks and an increase  
385 in FWHM when the molar water to the solute ratio (WSR) in  $\text{MgSO}_4$  and  $\text{Mg}(\text{NO}_3)_2$  particles decreases  
386 to less than six, the number of hydration of  $\text{Mg}^{2+}$  ions (Zhang and Chan, 2000; Zhang et al., 2004). These  
387 observations were attributed to direct contacting ion pairs formed between  $\text{Mg}^{2+}$  and anions, without  
388 water molecules between the ions. Besides, single-particle Raman spectroscopic analysis can reveal the  
389 structural heterogeneity of droplets. Raman imaging suggested that the  $\text{NO}_3^-$  to  $\text{Mg}^{2+}$  ratio of the contact  
390 ion pairs increases but the  $\text{H}_2\text{O}$  to  $\text{Mg}^{2+}$  ratio decreases as the surface of a highly supersaturated droplet

391 is approached (Zhang et al., 2004). Yeung and Chan (2010) reported that though no crystallization was  
392 shown by glyoxylic acid particle even at 0% RH, a new C=O peak at  $\sim 1820\text{cm}^{-1}$  appeared together with  
393 the aqueous C=O peak at  $1735\text{ cm}^{-1}$ , possibly indicating the presence of anhydrate (Yeung and Chan,  
394 2010).

395

### 396 **3.4 Liquid-liquid phase separation**

397 As mentioned above, partial crystallization can lead to a separation of solid and liquid mixed phases.  
398 Separation of two or even more liquid phases, namely liquid-liquid phase separation (LLPS), is also  
399 possible (Song et al., 2012a; Song et al., 2018; Huang et al., 2021; Ma et al., 2021). LLPS can be triggered  
400 by the interactions between inorganic, organic solutes and particulate water in mixed particles (You  
401 et al., 2012; Renbaum-Wolff et al., 2016). This phenomenon is mainly attributed to the low solubility  
402 of some non-polar or weakly polar organics, especially in the presence of inorganic salts, which  
403 may further decrease the solubilities of organics as the salting-out effects (Setschenow, 1889).

404

405 Optical microscopy (as a part of a single particle Raman microscope) can directly indicate LLPS by the  
406 contrasting colors on appearance, based on the different refractive indices of materials in different phases  
407 (You et al., 2012). Single-particle (micro-) Raman spectroscopy can examine LLPS via spatial scanning  
408 (micro-Raman), optical imaging (micro-Raman), Raman imaging, and whisper gallery modes (WGMs)  
409 with additional chemical information of the different phases (Bertram et al., 2011; Song et al., 2012b).  
410 Spatial scanning records distinct micro-Raman spectra at different locations of the particle and  
411 reveals LLPS (Bertram et al., 2011; Wu et al., 2018a) such as core-shell structures (e.g., an aqueous  
412 core surrounded by a BC-containing organic shell) (Brunamonti et al., 2015). However, Raman  
413 spatial scanning requires accurate focusing of the laser onto different targeted phases, which can be  
414 difficult when phases are separated into multiple small inclusions (Buajarem et al., 2007b).

415

416 Using spatial scanning and optical imaging, Ma et al. (2021) reported an organic shell-aqueous core  
417 LLPS in deposited 1, 2, 6-hexanetriol/ammonium sulfate mixed particles. However, different  
418 substrates for deposited particles could affect their LLPS behavior (Ma et al., 2021). Though LLPS  
419 of an organic/AS mixed particle has been observed on both hydrophobic (i.e., PTFE) and  
420 hydrophilic (i.e., glass) substrates, the former shows an organic shell with an AS inner core while

421 the latter shows an opposite configuration (Zhou et al., 2014b). To eliminate interaction with  
422 substrates, Ishizaka et al. (2021) used levitated droplets and found both core-shell and partially  
423 engulfed LLPS. The observed configurations of two phases are well consistent with thermodynamic  
424 predictions based on interfacial tensions and relative volume ratios of two immiscible phases  
425 (Ishizaka et al., 2021).

426

427 Another approach for identifying LLPS is Raman imaging of the whole particle in one single  
428 measurement. Typical Raman measurements bin the vertical pixels of a CCD to enhance the signal to  
429 noise ratio while the horizontal pixels represent the wave number after chromatic dispersion by a grating.  
430 Zhang et al. (2004) used collection optics to obtain an image of a particle in an EDB on the slit of a  
431 monochromator. Instead of using vertical binning, the vertical pixels registered the vertical profile of the  
432 Raman scattering (e.g., edge to center to edge) of the particle (Zhang et al., 2004). Chu and Chan (2017)  
433 reported that the core-shell phase separation in a mixed sucrose-ammonium sulfate particle with a sucrose  
434 molar fraction of 50% at <5% RH, but not at 70%RH. As shown in Fig. 3a, b (<5% RH), the accumulated  
435 C-H signal on the two sides indicates the presence of an organic-rich coating and an organic-deficient  
436 core. In contrast, the even distribution of the C-H signal in Fig. 3c (70% RH) suggests that the particle  
437 is likely homogeneous (Chu and Chan, 2017a). Kalume et al. (2018) observed temporally resolved LLPS  
438 in a diethyl phthalate and glycerol mixed droplet. Upon evaporation, diethyl phthalate migrated to the  
439 surface and formed an outer layer and glycerol was more concentrated in the interior of the droplet  
440 (Kalume et al., 2018).

441

442 Additionally, WGMs have also been utilized to infer the occurrence of LLPS and the specific  
443 particle morphologies. For example, different resonance structures appear in the Raman spectra  
444 when core-shell or engulfed phase separation occur (Buajareern et al., 2007a, b; Kwamena et al.,  
445 2010; Song et al., 2013; Marcolli and Krieger, 2020). Sharps peaks generated by WGMs in spectra can  
446 be found if the spatial distribution of particulate species is symmetric, such as those in core-shell  
447 separated and homogeneously mixed particles though the number, location, and intensity of WGMs  
448 peaks are different. In contrast, the engulfed phase-separated particles do not show any WGMs  
449 peaks (Sullivan et al., 2020). Utilizing WGMs, Stewart et al. (2015) reported the transition between  
450 partially-engulfed and core-shell structure at different RH values (Stewart et al., 2015). However,

451 these analyses focus on WGMs but not Raman as a chemical probing technique.

452

### 453 **3.5 Determination of pH**

454 The pH, defined as the activity of proton in aerosol particles, can also be inferred from Raman spectra  
455 based on the intensity of the conjugate acid/base ion pairs. Sulfate/bisulfate has been used most frequently.

456 The pH can be determined by substituting the conjugate ion pair concentrations and its dissociation  
457 coefficient into Henderson-Hasselbalch (H-H) (Radić and Prkić, 2012), Debye-Hückel theory, and  
458 specific ion interaction theory equations, respectively (Ciavatta, 1980; Rindelaub et al., 2016; Craig et al.,  
459 2017; Craig et al., 2018; Coddens et al., 2019; Chang et al., 2020a). The latter two are more suitable to

460 supersaturated particles since non-ideality has been considered. Rindelaub et al. (2016) reported direct  
461 measurements of pH in individual deposited particles according to sulfate/bisulfate peaks in Raman  
462 spectra, and its variation with RH (Rindelaub et al., 2016). Craig et al. (2017) extended this approach to

463 a range of atmospherically relevant inorganic and organic acid-base equilibria systems covering a wide  
464 range of pH (-1~10) (Craig et al., 2017). To eliminate the artifact of contacts between the particle and

465 the substrate, Coddens et al. (2019) determined the pH of trapped particles via titration by coalescence  
466 of droplets containing strong acids (Coddens et al., 2019). Boyer et al. (2020) further utilized the WGMs

467 for determining the solute concentration in real-time and achieve uncertainties in pH measurements of  
468 picoliter droplets ranging from  $\pm 0.03$  to 0.06 pH units (Boyer et al., 2020). Very recently, Cui et al. (2021)

469 reported that water can be used to probe pH in individual model aerosol particles (e.g.,  $(\text{NH}_4)_2\text{SO}_4$ , NaCl),  
470 since the water bands are affected by other components (e.g., ions), as discussed in Sec.3.3. Specifically,

471 the broad water peak at  $2600\text{-}3800\text{ cm}^{-1}$  could comprise many overlapping peaks, representing O-H  
472 vibration of water molecules in different local environments. The addition of solutes affects the local

473 environment of water molecules, and changes the relative intensities of the overlapped peaks. Hence, the  
474 activity of specific solutes can be obtained by analyzing the overlapped water peaks after rigorous

475 calibration; and the pH of the aerosol particle can be calculated (Cui et al., 2021).

476

### 477 **4 Multiphase reactions**

478 In Section 3, applications of characterizing single particles have been reviewed. This section mainly  
479 focuses on the "processes" occurring on single particles. Taking water-solute interactions as an example,

480 hygroscopicity describes the ability of solutes to absorb water upon equilibrium at fixed RH. Water



481 uptake is a dynamic process, although it is generally too quick to be a limiting step in most atmospheric  
482 applications. However, in some viscous matrixes, the water uptake rate could be reduced by orders of  
483 magnitude due to the limited diffusion (Chang et al., 2020b). Taking advantage of the different Raman  
484 characteristics of D<sub>2</sub>O and H<sub>2</sub>O, Davies and Wilson (2016) measured the diffusion coefficients of water  
485 molecules in trapped viscous particles by monitoring the isotopic exchange rate using Raman  
486 spectroscopy (Davies and Wilson, 2016). Determination of kinetic parameters of non-reactive processes  
487 such as partitioning coefficient, diffusion coefficient, and mass accommodation coefficient has been  
488 reviewed in another paper (Krieger et al., 2012). Hence, applications on probing multiphase reactions  
489 using single-particle Raman spectroscopy will be the focus below.

490

#### 491 **4.1 Multiphase formation of secondary inorganic aerosols (SIA)**

492 Particulate sulfate and nitrate are two major secondary inorganic aerosols (SIA). They have dominant  
493 Raman peaks at  $\sim 980\text{ cm}^{-1}$  and  $\sim 1046\text{ cm}^{-1}$ , respectively. Probing multiphase formation of sulfate by  
494 single-particle Raman spectroscopy was first employed by Davis and co-workers for absorption of SO<sub>2</sub>  
495 by alkali-metal hydroxides particles (Aardahl and Davis, 1996). In atmospheric applications, particulate  
496 sulfate formation has been a debating topic since the currently proposed pathways, including O<sub>3</sub>, OH  
497 radical, NO<sub>2</sub>, H<sub>2</sub>O<sub>2</sub>, and transition metal ions (TMI) in cloud water, cannot entirely account for the high  
498 concentration of sulfate observed in haze events such as those in the North China Plain (NCP) (Cheng et  
499 al., 2016). Using single-particle micro-Raman spectroscopy, Chan and his group reported that oxidants  
500 including NO<sub>2</sub>, N(III), OH radicals, etc., generated from particulate nitrate photolysis could effectively  
501 oxidize SO<sub>2</sub> to sulfate (Gen et al., 2019b; Gen et al., 2019c; Zhang et al., 2020a; Zheng et al., 2020b). Clear  
502 increase of the sulfate peak signal was identified in Raman spectra of UV irradiated nitrate particle (Fig.  
503 4). Later, they also reported sulfate formation by multiphase oxidation of SO<sub>2</sub> during FeCl<sub>3</sub> photolysis  
504 (Gen et al., 2020). [Angle et al. \(2021\)](#) reported an enhanced sulfate formation in TMI-containing droplets  
505 compared to that in TMI bulk solutions. This enhancement is greater than that can be explained by the  
506 higher TMI/bisulfite concentrations in aerosol than in bulk. It suggests that surface effects and potentially  
507 aerosol pH gradients play important roles in the S(IV) oxidation process in aqueous aerosols ([Angle et  
508 al., 2021](#)).

509

510 The formation of nitrate has also been investigated. Zangmeister and Pemberton (2001) performed

511 kinetic analysis on the reactions between deposited NaCl particles and gaseous HNO<sub>3</sub> based on the  
512 increase of the nitrate peak (Zangmeister and Pemberton, 2001). Tang et al. (2014) coupled optical  
513 levitation with Raman spectroscopy to investigate N<sub>2</sub>O<sub>5</sub> uptake on SiO<sub>2</sub> particle as a function of RH and  
514 found that particulate nitrate formation increased as RH increased. They conclude that the water content  
515 affects the partitioning of HNO<sub>3</sub> between the gas phase and condensed phases (i.e., adsorbed phase and  
516 aqueous phase). More surface adsorbed water layers block the reactive sites for N<sub>2</sub>O<sub>5</sub> uptake but promote  
517 HNO<sub>3</sub> dissolution (Tang et al., 2014). Scolaro et al. (2009) studied the three-dimensional evolution of  
518 the NaCl(100) surface during its reaction with NO<sub>2</sub> as a function of RH, using confocal Raman imaging  
519 combined with non-contact atomic force microscopy (AFM) (Scolaro et al., 2009). At 0% RH, a NaNO<sub>3</sub>  
520 monolayer capping the NaCl(100) surface formed. NaNO<sub>3</sub> tetrahedral crystals (<0.5 μm) formed at 45%  
521 RH, and supermicron NaNO<sub>3</sub> rhombohedral plates were obtained under the H<sub>2</sub>O multilayer regime  
522 (45%<RH<75%). At RH>80%, both crystalline and aqueous NO<sub>3</sub><sup>-</sup> were found. Reactions were  
523 accelerated in the presence of water vapor due to the formation of reactive HNO<sub>3</sub> by NO<sub>2</sub> hydrolysis.  
524 Ault et al. (2014) reported that individual nascent sea spray aerosol particles showed different reactivity  
525 toward HNO<sub>3</sub> and N<sub>2</sub>O<sub>5</sub>, likely due to compositional heterogeneity. After the same exposure of gaseous  
526 reactants, some particles showed intense ν(NO<sub>3</sub><sup>-</sup>) peak, whereas ν(C-H) is still the dominant mode in  
527 some other particles (Ault et al., 2014).

528

529 There are also investigations on the simultaneous formation of particulate sulfate and nitrate. Zhao et al.  
530 (2018) reported a multi-step reaction mechanism of oxidation of SO<sub>2</sub> by NO<sub>2</sub> on deposited CaCO<sub>3</sub>  
531 particles (Zhao et al., 2018). Further, Yu and Zhao et al. (2018) reported that the uptake coefficient of SO<sub>2</sub>  
532 on CaCO<sub>3</sub> particles in the presence of O<sub>2</sub>/NO<sub>2</sub> mixture was much higher than that without O<sub>2</sub> (Yu et al.,  
533 2018). The synergy of NO<sub>2</sub> and O<sub>2</sub>, which involved mechanisms such as chain reactions, resulted in much  
534 faster sulfate formation than the sum of the reaction rates with NO<sub>2</sub> and with O<sub>2</sub> alone. These reports  
535 show the usefulness of single-particle Raman spectroscopy in studying the multiphase formation of  
536 particulate sulfate and nitrate. It is worth mentioning that degradation of organo-sulfate has been  
537 proposed to produce particulate inorganic sulfate recently (Xu et al., 2020b) and organo-sulfate  
538 functional groups are also Raman-active (Bondy et al., 2018). Raman spectroscopy may find applications  
539 in the study of organo-sulfates.

540

## 541 **4.2 Multiphase formation of SOA**

542 Most of the organic compounds are Raman-active though some of them may not have strong signals.  
543 Some generate fluorescence in general orders of magnitude stronger than Raman emissions, masking  
544 useful Raman features of particles. The characteristic peaks of a single organic compound are generally  
545 more than that of an inorganic one due to its complex molecular vibration modes, and the reaction  
546 products may further complicate spectra analysis. Therefore, investigation on the multiphase formation  
547 of SOA by Raman spectroscopy is limited. However, though identifying the molecular nature of the  
548 products is difficult, single-particle Raman spectroscopy can provide useful information during  
549 secondary organic aerosol (SOA) formation. For example, Lee et al. (2008) observed a gradually  
550 elevating baseline in Raman spectra during acid-catalyzed octanol uptake by levitated sulfuric acid  
551 particles at 10% RH but not at 50% RH (Lee et al., 2008b). Though the speciation of products could not  
552 be resolved, the increasing fluorescence is evident, attributable to the formed SOA in the particles. Using  
553 an EDB, Chan and Chan (2011) examined the dependence of nonanal on the presence of hydrophilic and  
554 hydrophobic organics in acidic mixed organic-sulfuric acid particles. The presence of hydrophobic  
555 organic materials (oleic acid and its reaction products with sulfuric acid) enhanced SOA formation by  
556 reactive uptake of nonanal, likely through an enhanced dissolution of nonanal in the particles (Chan and  
557 Chan, 2011). In contrast, levoglucosan, a hydrophilic organic, did not increase the uptake coefficient of  
558 nonanal. It is suggested that acid-catalyzed reactive uptake should be examined with the explicit  
559 consideration of the role of particle-phase organics that are either initially present or accumulated as a  
560 reaction product. Using micro-Raman, Olson et al. (2019) investigated the uptake of isoprene epoxydiol  
561 (IEPOX) by  $\alpha$ -pinene SOA/toluene SOA-coated AS particles (Olson et al., 2019). Before the uptake,  
562 both coated AS particles show core-shell morphology.  $\nu(\text{N-H})$  and  $\nu(\text{SO}_4^{2-})$  were found at  $\sim 3200\text{cm}^{-1}$  and  
563  $\sim 976\text{cm}^{-1}$  in the particle core, while strong  $\nu(\text{C-H})$  at  $2800\text{-}3000\text{cm}^{-1}$  and other moderate/weak stretches  
564 of C-H were found in the shell region. After the uptake,  $\nu(\text{C-H})$  and  $\nu(\text{RO-SO}_3)$  were found in the particle  
565 core, indicating SOA formation, such as organo-sulfate. No organo-sulfate was detected in shell regions  
566 of both types of particles, although decreases of  $\nu(\text{C-H})$  peak were apparent. Generally, Raman analysis  
567 is useful for kinetic analysis of reactions (e.g., measuring uptake coefficients), but it is challenging to  
568 reveal complicated mechanisms due to the limited molecular identification. For better examining the  
569 reaction mechanism, deposited particles can be extracted for off-line analysis using mass spectrometry  
570 (MS) (Li et al., 2008; Chan et al., 2013).

571

### 572 **4.3 Multiphase oxidation of aerosol particles**

573 In addition to reactive uptake of SOA precursors, single-particle Raman spectroscopy has also been used  
574 to explore the uptake of oxidants by organic aerosol particles. So far, the reported studies are limited to  
575 ozonolysis. Raman spectroscopy is well suited in ozonolysis studies because the C=C bonds and the  
576 peroxide groups are Raman-active, and ozonolysis does not generate strongly fluorescent products.  
577 Using single-particle Raman spectroscopy, Lee and Chan (2007) performed in-situ observations of the  
578 particle mass, hygroscopicity, morphology of the oleic acid (Lee and Chan, 2007a), linolenic acid, and  
579 linoleic acid particles (Lee and Chan, 2007b) during ozonolysis. They found that low ozone concentration  
580 (~200–250 ppb) with a longer exposure period (20 h) favors autoxidation to form C=C–C=C groups;  
581 but an extremely high ozone concentration (~10 ppm) at shorter exposure time (2 h) tends to form  
582 carboxylic acids (C=O), secondary ozonide (O-O), hydroxyalkyl hydroperoxide (O-H), etc (Enami and  
583 Colussi, 2017; Qiu et al., 2020). Chu et al. (2019) further examined the interchangeability between ozone  
584 concentration and exposure time by studying ozonolysis of linoleic acid particles in a broader range of  
585 experimental conditions. They found the interchangeability holds at ozone exposure  $\leq 500$  ppb h and  $[O_3]$   
586  $\leq 100$  ppb for the formation of autoxidation products containing conjugated diene structures but does not  
587 hold for the decay of parent linoleic acid or at higher  $[O_3]$  (Chu et al., 2019). These results indicate that  
588 extrapolating experimental results of the ozonolysis under high  $[O_3]$  conditions to ambient levels should  
589 be carried out with caution. Single-particle Raman spectroscopy also enables us to infer the volatilization  
590 of some ozonolysis products. For example, Lee and Chan (2007) found that the mass of oleic acid  
591 particles was observed to decrease with time while that of linoleic acid and linolenic acid increased on  
592 the contrary, which could be potentially explained by the different volatility of the ozonolysis products  
593 (Lee and Chan, 2007b). King et al. (2004) reported an optical tweezers study of ozonolysis of oleic acid  
594 and synthetic seawater droplets. They found clear Raman signatures indicating nonanoic acid and  
595 nonanal production, followed by their gradual disappearance, which is also likely due to the volatilization  
596 (King et al., 2004). Furthermore, Dennis-Smith et al. (2012) used optical tweezers to study the  
597 oxidation of oleic acid droplets containing an inorganic seed with a time-resolution of 1 s to resolve the  
598 reactive loss of ozone and the evaporative loss of products. The oleic acid ozonolysis was completed in  
599 ~3000 s, but the decrease of droplet volume still lasts for an additional ~5000 s due to the slow  
600 volatilization of the products (Dennis-Smith et al., 2012).

601

602 Chan and Chan (2012) studied the roles of the phase state and water content in the ozonolysis of maleic  
603 acid (MA) and AS mixed particles. Aqueous MA was found to be more reactive toward ozone than  
604 crystalline MA. Interestingly, they also found that higher water content favors more efficient ozonolysis,  
605 although the concentration of MA is accordingly lower (Chan and Chan, 2012). Furthermore, ozonolysis  
606 of optically trapped bioaerosol particles has also been reported. In general, lipids and proteins show  
607 distinct  $\nu(\text{C-H})$  peaks at  $2855\text{ cm}^{-1}$  and  $2928\text{ cm}^{-1}$ , respectively (Kline and Treado, 1997; Rygula et al.,  
608 2013; Czamara et al., 2015). The ratio of these peaks can be thus used for inferring the different  
609 susceptibilities of lipids and proteins during ozonolysis oxidation (Gong et al., 2019). The products  
610 derived from oxidations such as carbonyls ( $\text{C=O}$ ;  $\sim 1700\text{ cm}^{-1}$ ) (Lee and Chan, 2007b) and oligomer of  
611 cysteine ( $\text{C-S}$ ;  $\sim 662\text{ cm}^{-1}$ ) (Movasaghi et al., 2007; Kampf et al., 2015) are also detected.

612

613 There are also studies exploring other organic surrogates of atmospheric aerosol with more complicated  
614 structures. For example, King et al. (2008) measured the uptake coefficients of ozone on fumarate and  
615 benzoate droplets (as a proxy of HULIS-containing aerosol) and  $\alpha$ -pinene droplets (a proxy of biogenic  
616 organic aerosol) (King et al., 2008). Different reaction products such as carbonate were identified in  
617 Raman spectra, though the chemical characterization is not comprehensive due to their volatility and the  
618 detection limits. The reaction of  $\alpha$ -pinene in the droplet phase was more than one order faster than in  
619 bulk aqueous solutions, likely due to more effective diffusion of ozone in the gas phase and more efficient  
620 mass accommodation at the air-droplet interface (King et al., 2008). [Milsom et al. \(2021\) reported the  
621 ozonolysis of fatty acid-soap mixed particles, using oleic acid and sodium oleate as models. In these  
622 particles, the strong interactions between the soap carboxylate and the carboxylic acid form crystalline  
623 structures \(Milsom et al., 2021\). Upon ozonolysis, the decay of  \$\text{C=C}\$  \( \$\sim 1600\text{ cm}^{-1}\$ \) was faster in liquid  
624 oleic acid droplets than crystalline oleic acid-soap particles, although the crystalline structure was  
625 eventually broken by ozonolysis. Uraoka et al. \(2017\) studied the multiphase reactions of optically-  
626 trapped soot particles with ozone and OH radicals.  \$\text{C=O}\$  vibrations were observed under both ozone and  
627 OH exposure. The graphitic domain was suggested to undergo OH oxidation based on the increase in the  
628 ratio of the disorder \(D\) to the graphite \(G\) domain from Raman spectra \(Uraoka et al., 2017\).](#)

629

630 **4.4 Amine/Ammonia reactions**

631 Ammonia and amines are the most abundant alkaline gases in the atmosphere. They play a significant  
632 role in new particle formation and buffering aerosol pH by neutralization of acidic particles (Kirkby et  
633 al., 2011;Almeida et al., 2013;Zhang et al., 2015;Kerminen et al., 2018;Zheng et al., 2020a). There are  
634 three types of reactions involving ammonia and amines: (1) Neutralization reaction between acidic  
635 particles and ammonia/amines; (2) Displacement of ammonia by amines from ammonium salt particles  
636 and vice versa from aminium salt particles; (3) Reactions between ammonia/amines and dissolved di-  
637 carbonyls or between gaseous di-carbonyls and ammonium/aminiium salt particles, both would result in  
638 the formation of colored compounds (i.e., Brown carbon; BrC).

639

640 Based on the strong vibration signal of the C-H bond ( $\sim 2900\text{cm}^{-1}$ , sharp peak) from amine/aminiium salts  
641 and the N-H bond ( $\sim 2800\text{-}3300\text{ cm}^{-1}$ , broad peak), the uptake of amine and ammonia can be easily studied  
642 using single-particle Raman spectroscopy. Sauerwein and Chan (2017) explored the role of phase state  
643 in simultaneous uptake of ammonia and dimethylamine (DMA) by acidic particles (e.g., sulfuric acid  
644 and oxalic acid) (Sauerwein and Chan, 2017). Anhydrous acidic particles were inert and took up DMA  
645 and ammonia presumably by adsorption only. The uptake rates of DMA and ammonia by aqueous acidic  
646 droplets were found comparable initially, but once the droplets were neutralized, the stronger base DMA  
647 displaced some of the particulate ammonium. On the other hand, if crystallization took place during the  
648 uptake, DMA uptake was inhibited, but continuous ammonia uptake gradually displaced the particle  
649 DMA ions.

650

651 Chan and Chan (2013) reported that the exchange reactions of ammonia/amine vapors in aqueous  
652 particles were reversible, and the exchange rates of aqueous particles were, in general, higher than those  
653 of their corresponding solid counterparts. Compared with crystalline solids (e.g., methylammonium  
654 sulfate), amorphous solid (e.g., diethylammonium sulfate) was found with a higher exchange rate, likely  
655 due to the less compact molecular structure (Chan and Chan, 2013). Chu and Chan (2017) further  
656 examined the effect of a hydrophilic viscous organic surrogate and a hydrophobic organic coating on  
657 DMA uptake by AS. Both the viscous materials and the fresh and aged organic coating retarded DMA  
658 uptake by mass transfer limitation (Chu and Chan, 2017b, a). The uptake of DMA by crystalized AS  
659 particles at 10-30% RH resulted in the deliquescence of the particles, likely due to the presence of surface  
660 adsorbed water (SAW) that promoted the dissolution of DMA. Once dimethylaminiium sulfate is formed,

661 it absorbs more water since it is more hygroscopic than AS and further promoted DMA uptake (Chu and  
662 Chan, 2017a). As crystalline solids are generally considered inert towards reactions, this finding indicates  
663 that SAW on crystals can serve as a medium to facilitate gas uptake.

664

665 BrC has attracted increasing attention due to its atmospheric abundance and capacity in regulating  
666 radiative balance (Laskin et al., 2015). The reactions between dicarbonyls and ammonium/ammonium-  
667 containing salt particles can form BrC. Gen et al. (2018) investigated the multiphase uptake of glyoxal  
668 by ammonium salt-containing particles using Micro-Raman spectroscopy. They found a gradual  
669 elevation of the baseline, which was attributed to the formation of a fluorescent BrC (i.e., 2,2'-  
670 biimidazole, BI), based on off-line analysis by UV-VIS spectroscopy and fluorescence spectroscopy  
671 (Gen et al., 2018a). The reduction in ALW at low RH increases the glyoxal uptake rate via the enhanced  
672 "salting-in" effect and the BI formation rate by facilitating dehydration reactions. Mabato et al. (2019)  
673 examined glyoxal uptake by methylammonium salt-containing particle. Although the "salting-in" effect  
674 was also found in methylammonium salt-containing particles, enhanced BI formation was not observed,  
675 likely due to the higher hygroscopicity of methylammonium salt (i.e., higher ALW content) than ammonium  
676 salt (Mabato et al., 2019).

677

#### 678 **4.5 Photochemistry of aerosol particles**

679 A particular type of aerosol particle reaction that deserves special attention is photochemical reactions,  
680 which can be initiated by irradiation of the particles. Nitrate can be photolyzed under atmospheric  
681 irradiation ( $\lambda > 290\text{nm}$ ). Nitrate photolysis proceeds via three channels: one produces  $\text{NO}_2$  and OH  
682 radicals, another produces  $\text{NO}_2^-$  and  $\text{O}(^3\text{P})$  and the last generates ONOO $\cdot$ . The third channel's quantum  
683 yield is considered negligible compared with the former two since ONOO $\cdot$  is unstable. It has been  
684 reported that  $\text{NO}_2^-$  and ONOO $\cdot$  peaks increased, but  $\text{NO}_3^-$  peaks decreased in the Raman spectra of  
685 acoustically levitated nitrate particles irradiated by UV (Tobon et al., 2017).  $\text{NO}_2$  does not have a large  
686 absorption cross-section, but it may be hydrolyzed into  $\text{NO}_2^-$  (Tobon et al., 2017; Seng et al., 2018; Gómez  
687 Castaño et al., 2019). Most nitrate photolysis products are oxidants, so their ability to initiate oxidation  
688 reactions has also been explored (Gen et al., 2019b; Gen et al., 2019c; Zhang et al., 2020a). The production  
689 of sulfate via nitrate photolysis was discussed earlier. Recently, Zhang et al. (2021) reported a prominent  
690 formate production by glyoxal oxidation during particulate nitrate photolysis, instead of the more

691 commonly found oxalic acids oligomers in the oxidation of glyoxal in bulk solutions (Zhang et al.,  
692 2021b). Furthermore, Liang et al. (2021) reported nitrate photolysis in particles containing sucrose,  
693 which was used as a surrogate for atmospheric viscous organics. They found that the viscosity of the  
694 particle did not reduce the nitrate photolysis rate, but it limited the diffusion of gaseous products (e.g.,  
695 NO<sub>x</sub>, NO<sub>y</sub>) from nitrate photolysis. At a high sucrose fraction and 30%RH, the production of these  
696 gaseous products and the particles' viscosity transformed the droplets into “hollow and enlarged” semi-  
697 solid particles (Liang et al., 2021).

698

699 Size dependence of nitrate photochemistry has been recently reported, based on single-particle Raman  
700 spectroscopy. Tobon et al. studied photolysis acoustically levitated nitrate particles (40~80μm) at 254nm  
701 UV radiation. No change in Raman spectra for 2 h. In contrast, smaller particles (5~8μm) trapped  
702 optically yielded various Raman peaks of nitrate photolysis products (Tobon et al., 2017;Gómez Castaño  
703 et al., 2019). The slow photolysis in the larger nitrate particles was attributed to the self-inhibited surface  
704 process. Additionally, an uneven distribution of NO<sub>2</sub><sup>-</sup> inside the smaller particle was also observed  
705 through Raman mapping (Gómez Castaño et al., 2019). Organics in the aerosol particle may also  
706 decompose under light. For example, Parmentier et al. reported photodegradation of optically trapped  
707 oleic acid droplets under 532 nm and 660 nm irradiation, likely initiated by photosensitization. However,  
708 they cautioned that degradation loss of optically trapped particles might be artifacts (Parmentier et al.,  
709 2021). The photo-decay of light-absorbing particulate matters is also of great interest in understanding  
710 their fate in the atmosphere. However, there are very limited studies of atmospheric photochemical  
711 reactions using Raman spectroscopy, partly because of the need for complementary chemical speciation  
712 for detailed mechanistic studies.

713

#### 714 **5 Enhanced Raman spectroscopy**

715 Though Raman has been used to study physical and chemical processes of atmospheric particles, most  
716 of the studies used large particles (dozens of microns) and focused on lab-generated particles with a few  
717 representative components. That is primarily because of the intrinsic diffraction limitation of Raman  
718 measurements that the laser beam cannot be effectively focused to a spot smaller than its wavelength and  
719 thus limits the detection of particles to larger than 1 micron or so. Fluorescence can also be a complication  
720 in some chemical systems.



721

722 Various methods have been developed to improve the Raman signal-to-noise ratios and the spatial  
723 resolution in other research fields such as material science and biology. Surface-enhanced Raman  
724 spectroscopy (SERS) and Tip-enhanced Raman spectroscopy (TERS) have been recently employed in  
725 atmospheric research. SERS and TERS enhance Raman emissions by the localized surface plasmon  
726 resonances using noble metal nanoparticles (NPs) to provide "hot spots" near the contacting sites between  
727 the analyte and NPs (Ault and Axson, 2017). According to the SERS electromagnetic (EM) enhancement  
728 theory, the relationship between the SERS intensity (I) and the local EM strength (E) follows  $I \propto |E|^4$ .  
729 The relationship between E and the distance between NPs and analytes (D) is described as  $E \propto (1/D)$   
730 (Zhou et al., 2015). Hence, maximizing E and minimizing D without inducing significant perturbation  
731 to the sample is the primary goal. In addition to this physical enhancement based on the electromagnetic  
732 field, Raman signals can also be enhanced chemically. Specifically, molecular/ionic species can attach  
733 to the surface of NPs, distorting the molecular structure and increasing the absorption cross-section.  
734 Consequently, the Raman signal of an adsorbed species can be enhanced, potentially accompanied by a  
735 peak shift (Craig et al., 2015; Gen and Chan, 2017).

736

737 SERS enables the measurements of single particles smaller than 1 micron. Craig et al. (2015) found that  
738 the signals from individual submicron (down to 0.6  $\mu\text{m}$ ) particles could be effectively detected with  
739 intensity enhancement (Craig et al., 2015). Furthermore, Tirella et al. (2018) extended the SERS  
740 detection to the accumulation mode (800~150 nm) particles (Tirella et al., 2018). Sun et al. (2019)  
741 reported a size-resolved (covering both coarse mode and accumulation mode) SERS characterization  
742 study of atmospheric particles sampled during haze events (Sun et al., 2019a; Sun et al., 2019b). More  
743 recently, Kuniyama et al. (2020) reported sensitive SERS measurement of Aiken mode particles (<100nm)  
744 by combining a condensational growth tube sampler (CGT) and a SERS substrate for directly sampling  
745 (Kuniyama et al., 2020). The wide analytical range of particle size enables SERS to be a potentially  
746 powerful tool in studying ambient particulate matters (Steer et al., 2016; Vejpongsa et al., 2017; Chen et  
747 al., 2021).

748

749 Some species including components of microorganisms (Tahir et al., 2020), microplastics (Xu et al.,  
750 2020a), crystalline silica (Zheng et al., 2018), the fine structure of organics (Craig et al., 2015; Fu et al.,

751 2017;Gen et al., 2018b), and even some Raman-active inorganic salts at very low concentration (Saniel  
752 et al., 2019) are invisible in normal Raman due to their weak Raman-activities. However, they could be  
753 detected with a SERS substrate. The sensitive detection by SERS can provide valuable insight into  
754 particle transformations and emission sources (Vejpongsa et al., 2017;Ghosal and Wall, 2019;Lee et al.,  
755 2019). However, the enhancement factor of SERS is not constant. It strongly depends on the distribution  
756 and quantity of noble metal NPs and the hotspots over the substrate, making quantitative analysis difficult.  
757 Many attempts have been made to explore preferable and tunable substrate for generalizable atmospheric  
758 particle detection (Xu et al., 2020a;Cheng et al., 2021), but still more progresses are needed in the future.

759

760 The most common SERS application uses particles deposited on SERS substrates, relying on the "hot  
761 spot" locating beneath the analyte particles. Recently, some studies create innovative interactions  
762 between particulate analytes and SERS NPs to enhance SERS detections. Wei et al. (2018) used 4-  
763 mercaptobenzoic acid-functionalized AuNPs as pH nanoprobe and internal SERS substrate and found  
764 the existence of a stable pH gradient inside aqueous particles (Wei et al., 2018). Hence, the assumption  
765 of homogeneous mixing might not always be correct, and pH predictions by thermodynamic model might  
766 underestimate the acidity of interfacial layers of particles, which is crucial for multiphase uptake or  
767 surface reactions. As a further investigation of the SERS pH nanoprobe, Huang et al. (2020) reported  
768 that the pH distribution inside aerosol particles is affected by the internal distribution of ions, which may  
769 depend on the ionic speciation. While sodium tends to reside in the bulk of the particle, leading to a high  
770 centroid pH, ammonium distributes more evenly due to its increased surface propensity (Huang et al.,  
771 2020).

772

773 Gen et al. developed an electrospray system (ES-SERS) to deposit SERS NPs onto the surface of the  
774 analyte particle and found that this technique can selectively enhance the peak intensity of the species  
775 located at surface layers such as surface adsorbed water (Gen and Chan, 2017) and organic coatings (Gen  
776 et al., 2019a). In a typical micro-Raman set-up, the objective is above the analyte particle. When the  
777 analyte particle is deposited on the SERS substrate, the SERS hot spots are located beneath the particle.  
778 In other words, upon laser irradiation from the top, the photons generated by excitation need to pass  
779 through the particle with a refractive index greater than air, which would scatter or absorb light and thus  
780 reduces the signals received by the Raman microscope. In contrast, ES-SERS hot spots are created on

781 the surface of the particle using electrospray. This configuration reduces the loss of photons and affords  
782 greater enhancement in the Raman intensity. (Fig. 5) Besides, as the SERS effect is much more prominent  
783 near the hot spots (i.e., small D), the location of the hot spots determines where will be probed in SERS  
784 spectra. Therefore, while typical SERS substrate collects enhanced Raman signals from the substrate-  
785 particle interface, the ES-SERS can provide information from the gas-particle interface, where many  
786 atmospheric multiphase processes occur. Sivaprakasam et al. reported real-time SERS measurements of  
787 electrostatically trapped particles containing analyte molecules and NPs as internally mixed liquid  
788 particles or coating on solid particles (Sivaprakasam et al., 2017; Sivaprakasam and Hart, 2021). The  
789 interaction between NPs and analyte increased due to more contact areas than that between an aerosol  
790 particle and a substrate.

791

792 Similarly, TERS can produce enhanced Raman signals even from particles in the nucleation mode. TERS  
793 is a combination of atomic force microscope (AFM) and Raman spectrometer. In general, AFM  
794 determines the topography of a single deposited particle by detecting the interaction force between the  
795 AFM tip and the surface of the analytes. In a typical TERS set-up, the AFM tip is coated with noble  
796 metal particles. An enhanced Raman signal is generated when the tip is interacting with analytes under  
797 laser excitation (Rodriguez et al., 2015). The lack of chemical information of AFM is complemented by  
798 SERS. Thus, TERS enables simultaneous characterization of particulate topography and surface species  
799 of submicron particles at a high spatial resolution (Ofner et al., 2016). TERS also has the potential for  
800 quantitative analysis since the quantity and configuration of hotspots on the tip are constant.

801

## 802 **6 Bioaerosols**

803 Bioaerosols have attracted increasing attention worldwide dramatically due to the COVID-19 epidemic.  
804 Studies using normal Raman/SERS for off-line detection of biological samples (Félix-Rivera and  
805 Hernández-Rivera, 2012; Mosier-Boss, 2017), real-time sensing of bioaerosol (Huffman et al., 2020)  
806 have been reviewed in detail elsewhere. Bioaerosols have various Raman active components such as  
807 phosphate lipid ( $\delta$  (=C-H),  $\sim 1268\text{cm}^{-1}$ ;  $\nu$ (C-H),  $\sim 2855\text{cm}^{-1}$ ), protein (amides bands,  $\sim 1260\text{cm}^{-1}$ ,  
808  $\sim 1600\text{cm}^{-1}$ ,  $\sim 1660\text{cm}^{-1}$ ; C-C backbone stretching in  $\beta$ -sheet proteins,  $\sim 983\text{cm}^{-1}$ ;  $\nu$ (C-H),  $\sim 2928\text{cm}^{-1}$ ) and  
809 nucleic acids (e.g., adenine,  $\sim 735\text{cm}^{-1}$ ), etc (Socrates, 2004; Rygula et al., 2013; Talari et al., 2015).  
810 However, Raman signals from bioaerosol particles are generally weak. To amplify the signals, bioaerosol

811 particles are trapped or deposited onto a substrate for longer integration time (Laucks et al.,  
812 2000;Sengupta et al., 2005;Tripathi et al., 2009;Wang et al., 2015a;Redding et al., 2015b;Ai et al., 2020).  
813 Using a higher energy laser can also enhance Raman intensity, but it may cause damage to bioaerosol  
814 (e.g., fragmentation) (Gong et al., 2017). On this basis, SERS is more suitable than normal Raman  
815 spectroscopy. SERS can also quench the fluorescence generated by biomolecules such as tryptophan and  
816 tyrosine (Gong et al., 2017).

817

818 In general, there are two strategies of single-particle SERS of bioaerosols: (1) directly sampling  
819 bioaerosols on a SERS substrate; (2) moving mixed colloids of SERS NPs and bioaerosols onto a glass  
820 substrate, followed by drying. While the former is more convenient without complex pretreatments  
821 (Tahir et al., 2020), the latter enables flexible modification of NPs properties. For example,  
822 functionalized surface of NPs with tag molecules (e.g., antibody), so-called label-based SERS (Liu et al.,  
823 2010), were used for detecting specific biomaterials with high reproducibility. Label-free SERS refers to  
824 that without tag molecules, such as Au@Ag. In general, by simply mixing, NPs distribute on biomaterials  
825 without specific interactions, and the SERS reproducibility is limited. However, by coating AgNPs on  
826 the cell wall of bacteria (Zhou et al., 2014a;Zhou et al., 2015), SERS enhancement was ~30-folds  
827 reproducibly higher than simply mixed colloid–bacterial suspension. Furthermore, the discrimination of  
828 live and dead bacteria was possible. NPs can be directly formed inside some specific bacteria via bio-  
829 reduction for probing the intercellular structure (Jarvis et al., 2008). Overall, SERS can be an innovative  
830 tool in bioaerosol characterization, but the antibacterial effect of NPs and heat effect due to excitation  
831 laser should be considered (Mosier-Boss, 2017). More examples of bioaerosol detection can be found in  
832 a recent review (Liu et al., 2017).

833

## 834 **7 Future directions**

835 This review paper has shown examples of single-particle Raman spectroscopy in studying atmospheric  
836 processes. Overall, the water content, phase state, morphology, and chemical composition of single  
837 particles during physical and chemical processes at controlled RH can be monitored in situ.  
838 Hygroscopicity and phase behaviors covering a wide range of RH after these processes can also be  
839 comprehensively assessed by performing evaporation-humidification cycle measurements (Chan et al.,  
840 2006;Chan and Chan, 2007;Liu et al., 2008;Chen et al., 2020). Although fluorescence may exist in some

841 particles, it could be potentially reduced or even eliminated by (1) using longer excitation wavelengths  
842 (e.g., 785 and 1064 nm); (2) employing SERS/TERS; (3) photo-bleaching of fluorescent substances  
843 under UV-VIS illumination.(Gong et al., 2017) There are many other innovative studies built on trapping,  
844 manipulating, and observing multi-particles via Raman (Mitchem and Reid, 2008;Davies, 2019), such as  
845 measuring viscosity and diffusion coefficient (Power et al., 2013;Nakajima et al., 2021), probing reaction  
846 (Aardahl, 1998;Rkiouak et al., 2014) and phase transition (Richards et al., 2020). Based on these  
847 functions and research progresses, we would like to provide the following suggestions on future  
848 directions:

849

850 ● **Hyphenated single-particle Raman spectroscopy.** Raman spectroscopy is non-destructive, so  
851 incorporating other spectroscopic techniques for characterizing the same particle is possible.  
852 Vibrational sum frequency generation spectroscopy (SFG), Fourier transform infrared spectroscopy  
853 (FT-IR), and fluorescence spectroscopy, which are also non-destructive, could be complementary  
854 to Raman in probing chemical composition of single particle. Recently, novel combination of EDB  
855 and mass spectrometry was reported, which can directly introduce the trapped particle for mass  
856 spectrometry analysis (Jacobs et al., 2017;Birdsall et al., 2018;Willis et al., 2020). Adaption of this  
857 technique with Raman to form an EDB – Raman system with subsequent MS analysis is relatively  
858 straight forward. For optical properties, UV/Vis spectroscopy could be a promising choice (Jones  
859 et al., 2021). While general laser-based MDR can easily bleach light-absorbing molecules, a recent  
860 study reported that MDR modes under broad band excitation can measure refractive index (RI) of  
861 light-sensitive samples (Price et al., 2020). Such MDR measurements can complement in-situ  
862 Raman spectroscopy for chemical characterization. Additionally, SERS/TERS are emerging useful  
863 approaches, but current SERS/TERS methods for atmospheric research mainly use bare NPs. The  
864 direct contact of NPs to analyte molecules can potentially induce chemical enhancement, which  
865 could complicate the identification of the phase transition and functional groups (Craig et al.,  
866 2015;Gen and Chan, 2017). To remove the chemical enhancement, future studies on chemically  
867 inert NPs such as shell-isolated nanoparticle-enhanced Raman spectroscopy (SHINERS) are  
868 suggested (Li et al., 2010;Anema et al., 2011).

869

870 ● **Multiphase reaction studies based on single-particle Raman spectroscopy.** Single-particle

871 Raman spectroscopy enables investigations of various atmospheric reactions, including those in  
872 surface adsorbed water for solids, mixed-phase particles (solid, aqueous, organic), supersaturated  
873 droplets, atmospheric aging of bioaerosols and ultrafast reactions. For solid particles (e.g.,  
874 crystalline, mineral dust), multiphase reactions can be “mediated” by surface adsorbed water layers  
875 and may result in phase transition, turning the particle into liquid for further reactions (Kuwata and  
876 Martin, 2012;Chu and Chan, 2017a;Zhao et al., 2018;Yu et al., 2018;Gen et al., 2019a). Probing  
877 heterogenous reactions on the particle surface is possible via ES-SERS, TERS, and normal Raman  
878 imaging. As particle constituents can be unevenly distributed (e.g., in LLPS) within a single particle,  
879 chemistry may not be the same between the bulk and the surface layers (Wei et al., 2018;Olson et  
880 al., 2019;Qiu et al., 2019;Huang et al., 2020;Lam et al., 2021). The studies of the atmospheric  
881 processing of pre-existing particles to form secondary aerosols can be further extended to the aging  
882 of bioaerosols (Gong et al., 2019). Using pulse laser for excitation, time-resolved resonance Raman  
883 spectroscopy (TR3) can be a promising tool in probing short-lived reactive intermediates (e.g.,  
884 triplet state molecules). In particular, it helps deepen our understanding in ultrafast reactions or  
885 initiation steps of typical reactions (Sahoo et al., 2011;Collins et al., 2018).

886

887 ● **Particle size and temperature effects.** Many publications report single-particle Raman  
888 spectroscopy studies under different environmental conditions, including RH and gas concentration,  
889 etc. However, how experimental conditions such as temperature and particle size affect kinetics and  
890 products in multiphase reactions remains ambiguous. For example, various pathways and kinetic  
891 parameters have been proposed to explain particulate sulfate formation in winter haze events in  
892 northern China (Chan and Yao, 2008;Su et al., 2020;Liu et al., 2021). However, most studies are  
893 based on experimental results at room temperature or 298K. Further exploration with respect to the  
894 effect of low temperature on the properties of the particles and multiphase sulfate chemistry is still  
895 warranted. Employing a temperature-controlled cold plate flow cell - Raman system for deposited  
896 single particles (Wheeler et al., 2015;Mael et al., 2019;Roy et al., 2020), investigations of  
897 temperature-dependent reaction kinetics can be easily achieved. Temperature control in a small  
898 levitation chamber is also more convenient than in a flow tube or smog chamber. To date, almost  
899 all single-particle Raman studies involve supermicron particles. While equilibrium measurements  
900 are not sensitive to size (assuming the Kelvin effect is considered), kinetic analysis is often size-

901 dependent. Hence, uptake coefficients for multiphase reactions are usually reported and are  
902 restricted to experimental conditions that gas and liquid phase transport are not the rate-limiting  
903 step. The size detection limit of single-particle Raman spectroscopy can be extended to sub-10  
904 micrometer with high sensitivity using high-energy excitation laser and tighter optical focusing.  
905 The effect of temperature and particle size on multiphase chemistry should be further investigated  
906 using long integration time, novel optical configuration (e.g., confocal micro-Raman), and  
907 SERS/TERS, etc. Although it is challenging to study single submicron particles by Raman  
908 spectroscopy regularly, Raman characterization of a collection of single submicron particles is  
909 feasible.

910

#### 911 **Acknowledgment:**

912 We gratefully acknowledge the supports from the National Natural Science Foundation of China (No.  
913 41905122, 42075100, and 41875142), the Hong Kong Research Grants Council (No.11302318), the  
914 Japan Science and Technology Agency (JST) for Fusion Oriented Research for disruptive Science and  
915 Technology program (20352853), the Japan Society for the Promotion of Science (JSPS) Grants-in-Aid  
916 for Early-Career Scientists (21K17876).

917

#### 918 **Reference**

- 919 Aardahl, C. L., and Davis, E. J. P. B.: Gas/Aerosol Chemical Reactions in the NaOH-SO<sub>2</sub>-H<sub>2</sub>O System,  
920 *Applied Spectroscopy*, 50, 71-77, 1996.
- 921 Aardahl, C. L. W. J. F. D. E. J.: Raman Analysis of Chemical Reactions Resulting from the Collision of  
922 Micrometer-Sized Particles, *Applied Spectroscopy*, 52, 47-53, 1998.
- 923 Ai, Y., Alali, H., Pan, Y.-L., Videen, G., and Wang, C.: Single-particle optical-trapping raman  
924 spectroscopy for the detection and identification of aerosolized airborne biological particles,  
925 *Measurement Science and Technology*, 10.1088/1361-6501/abd5f1, 2020.
- 926 Akimoto, H., Hoshino, M., Inoue, G., Sakamaki, F., Washida, N., and Okuda, M.: Design and  
927 characterization of the evacuable and bakable photochemical smog chamber, *Environmental  
928 Science & Technology*, 13, 471-475, 1979.
- 929 Almeida, J., Schobesberger, S., Kürten, A., Ortega, I. K., Kupiainen-Määttä, O., Praplan, A. P., Adamov,  
930 A., Amorim, A., Bianchi, F., and Breitenlechner, M.: Molecular understanding of sulphuric  
931 acid–amine particle nucleation in the atmosphere, *Nature*, 502, 359-363, 2013.
- 932 Anema, J. R., Li, J.-F., Yang, Z.-L., Ren, B., and Tian, Z.-Q.: Shell-Isolated Nanoparticle-Enhanced  
933 Raman Spectroscopy: Expanding the Versatility of Surface-Enhanced Raman Scattering,  
934 *Annual Review of Analytical Chemistry*, 4, 129-150, 10.1146/annurev.anchem.111808.073632,  
935 2011.

936 Angle, K. J., Neal, E. E., and Grassian, V. H.: Enhanced Rates of Transition-Metal-Ion-Catalyzed  
937 Oxidation of S(IV) in Aqueous Aerosols: Insights into Sulfate Aerosol Formation in the  
938 Atmosphere, *Environmental Science & Technology*, 55, 10291-10299, 10.1021/acs.est.1c01932,  
939 2021.

940 Ao, J., Feng, Y., Wu, S., Wang, T., Ling, J., Zhang, L., and Ji, M.: Rapid, 3D Chemical Profiling of  
941 Individual Atmospheric Aerosols with Stimulated Raman Scattering Microscopy, *Small*  
942 *Methods*, 4, 1900600, <https://doi.org/10.1002/smt.201900600>, 2020.

943 Ashkin, A.: Acceleration and Trapping of Particles by Radiation Pressure, *Physical Review Letters*, 24,  
944 156-159, 10.1103/PhysRevLett.24.156, 1970.

945 Ashkin, A., and Dziedzic, J.: Observation of optical resonances of dielectric spheres by light scattering,  
946 *Appl. Opt.*, 20, 1803-1814, 1981.

947 Ashraf, H., Guo, Y., Wang, N., Pang, S., and Zhang, Y.-H.: Hygroscopicity of Hofmeister Salts and  
948 Glycine Aerosols—Salt Specific Interactions, *The Journal of Physical Chemistry A*, 125, 1589-  
949 1597, 2021.

950 Ault, A. P., Guasco, T. L., Baltrusaitis, J., Ryder, O. S., Trueblood, J. V., Collins, D. B., Ruppel, M. J.,  
951 Cuadra-Rodriguez, L. A., Prather, K. A., and Grassian, V. H.: Heterogeneous Reactivity of  
952 Nitric Acid with Nascent Sea Spray Aerosol: Large Differences Observed between and within  
953 Individual Particles, *The Journal of Physical Chemistry Letters*, 5, 2493-2500,  
954 10.1021/jz5008802, 2014.

955 Ault, A. P., and Axson, J. L.: Atmospheric Aerosol Chemistry: Spectroscopic and Microscopic Advances,  
956 *Analytical Chemistry*, 89, 430-452, 10.1021/acs.analchem.6b04670, 2017.

957 Bao, F., Li, M., Zhang, Y., Chen, C., and Zhao, J.: Photochemical Aging of Beijing Urban PM<sub>2.5</sub>: HONO  
958 Production, *Environmental Science & Technology*, 52, 6309-6316, 10.1021/acs.est.8b00538,  
959 2018.

960 Batonneau, Y., Sobanska, S., Laureyns, J., and Bremard, C.: Confocal Microprobe Raman Imaging of  
961 Urban Tropospheric Aerosol Particles, *Environmental Science & Technology*, 40, 1300-1306,  
962 10.1021/es051294x, 2006.

963 Behnke, W., Holländer, W., Koch, W., Nolting, F., and Zetzsch, C.: A smog chamber for studies of the  
964 photochemical degradation of chemicals in the presence of aerosols, *Atmospheric Environment*  
965 (1967), 22, 1113-1120, 1988.

966 Bertram, A., Martin, S., Hanna, S., Smith, M., Bodsworth, A., Chen, Q., Kuwata, M., Liu, A., You, Y.,  
967 and Zorn, S.: Predicting the relative humidities of liquid-liquid phase separation, efflorescence,  
968 and deliquescence of mixed particles of ammonium sulfate, organic material, and water using  
969 the organic-to-sulfate mass ratio of the particle and the oxygen-to-carbon elemental ratio of the  
970 organic component, *Atmospheric Chemistry & Physics*, 11, 2011.

971 Birdsall, A. W., Krieger, U. K., and Keutsch, F. N.: Electrodynamic balance—mass spectrometry of single  
972 particles as a new platform for atmospheric chemistry research, *Atmospheric Measurement*  
973 *Techniques*, 11, 33-47, 2018.

974 Bondy, A. L., Craig, R. L., Zhang, Z., Gold, A., Surratt, J. D., and Ault, A. P.: Isoprene-Derived  
975 Organosulfates: Vibrational Mode Analysis by Raman Spectroscopy, Acidity-Dependent  
976 Spectral Modes, and Observation in Individual Atmospheric Particles, *The Journal of Physical*  
977 *Chemistry A*, 122, 303-315, 10.1021/acs.jpca.7b10587, 2018.

978 Boyer, H. C., Gorkowski, K., and Sullivan, R. C.: In Situ pH Measurements of Individual Levitated  
979 Microdroplets Using Aerosol Optical Tweezers, *Analytical Chemistry*, 92, 1089-1096,



980 10.1021/acs.analchem.9b04152, 2020.

981 Braban, C. F., Carroll, M. F., Styler, S. A., and Abbatt, J. P.: Phase transitions of malonic and oxalic acid  
982 aerosols, *The Journal of Physical Chemistry A*, 107, 6594-6602, 2003.

983 Brunamonti, S., Krieger, U. K., Marcolli, C., and Peter, T.: Redistribution of black carbon in aerosol  
984 particles undergoing liquid-liquid phase separation, *Geophysical Research Letters*, 42, 2532-  
985 2539, 2015.

986 Buajareern, J., Mitchem, L., and Reid, J. P.: Characterizing Multiphase Organic/Inorganic/Aqueous  
987 Aerosol Droplets, *The Journal of Physical Chemistry A*, 111, 9054-9061, 10.1021/jp074366a,  
988 2007a.

989 Buajareern, J., Mitchem, L., and Reid, J. P.: Characterizing the Formation of Organic Layers on the  
990 Surface of Inorganic/Aqueous Aerosols by Raman Spectroscopy, *The Journal of Physical  
991 Chemistry A*, 111, 11852-11859, 10.1021/jp075021v, 2007b.

992 Cai, C., and Zhao, C.: Optical levitation measurement on hygroscopic behaviour and SVOC vapour  
993 pressure of single organic/inorganic aqueous aerosol, *Atmospheric Environment*, 189, 50-60,  
994 <https://doi.org/10.1016/j.atmosenv.2018.06.040>, 2018.

995 Carey, D. M., and Korenowski, G. M.: Measurement of the Raman spectrum of liquid water, *The Journal  
996 of chemical physics*, 108, 2669-2675, 1998.

997 Chan, C. K., Flagan, R. C., and Seinfeld, J. H.: Resonance structures in elastic and Raman scattering  
998 from microspheres, *Appl. Opt.*, 30, 459-467, 10.1364/AO.30.000459, 1991.

999 Chan, C. K., Flagan, R. C., and Seinfeld, J. H.: Water activities of NH<sub>4</sub>NO<sub>3</sub>/(NH<sub>4</sub>)<sub>2</sub>SO<sub>4</sub> solutions,  
1000 *Atmospheric Environment. Part A. General Topics*, 26, 1661-1673,  
1001 [https://doi.org/10.1016/0960-1686\(92\)90065-S](https://doi.org/10.1016/0960-1686(92)90065-S), 1992.

1002 Chan, C. K., and Yao, X.: Air pollution in mega cities in China, *Atmospheric Environment*, 42, 1-42,  
1003 10.1016/j.atmosenv.2007.09.003, 2008.

1004 Chan, K. M., Huang, D. D., Li, Y. J., Chan, M. N., Seinfeld, J. H., and Chan, C. K.: Oligomeric products  
1005 and formation mechanisms from acid-catalyzed reactions of methyl vinyl ketone on acidic  
1006 sulfate particles, *Journal of Atmospheric Chemistry*, 70, 1-18, 2013.

1007 Chan, L. P., and Chan, C. K.: Enhanced Reactive Uptake of Nonanal by Acidic Aerosols in the Presence  
1008 of Particle-Phase Organics, *Aerosol Science and Technology*, 45, 872-883,  
1009 10.1080/02786826.2011.567314, 2011.

1010 Chan, L. P., and Chan, C. K.: Roles of the Phase State and Water Content in Ozonolysis of Internal  
1011 Mixtures of Maleic Acid and Ammonium Sulfate Particles, *Aerosol Science and Technology*,  
1012 46, 781-793, 10.1080/02786826.2012.665514, 2012.

1013 Chan, L. P., and Chan, C. K.: Role of the aerosol phase state in ammonia/amines exchange reactions,  
1014 *Environmental science & technology*, 47, 5755-5762, 2013.

1015 Chan, M. N., Choi, M. Y., Ng, N. L., and Chan, C. K.: Hygroscopicity of Water-Soluble Organic  
1016 Compounds in Atmospheric Aerosols: Amino Acids and Biomass Burning Derived Organic  
1017 Species, *Environmental Science & Technology*, 39, 1555-1562, 10.1021/es049584l, 2005.

1018 Chan, M. N., Lee, A. K., and Chan, C. K.: Responses of ammonium sulfate particles coated with glutaric  
1019 acid to cyclic changes in relative humidity: Hygroscopicity and Raman characterization,  
1020 *Environmental science & technology*, 40, 6983-6989, 2006.

1021 Chan, M. N., and Chan, C. K.: Mass transfer effects on the hygroscopic growth of ammonium sulfate  
1022 particles with a water-insoluble coating, *Atmospheric Environment*, 41, 4423-4433,  
1023 <https://doi.org/10.1016/j.atmosenv.2007.01.047>, 2007.

1024 Chang, P., Chen, Z., Zhang, Y., and Liu, Y.: Direct measurement of aerosol pH in individual malonic acid  
1025 and citric acid droplets under different relative humidity conditions via Raman spectroscopy,  
1026 *Chemosphere*, 241, 124960, 2020a.

1027 Chang, P., Gao, X., Cai, C., Ma, J., and Zhang, Y.: Effect of waiting time on the water transport kinetics  
1028 of magnesium sulfate aerosol at gel-forming relative humidity using optical tweezers,  
1029 *Spectrochimica Acta Part A: Molecular and Biomolecular Spectroscopy*, 228, 117727,  
1030 <https://doi.org/10.1016/j.saa.2019.117727>, 2020b.

1031 Charan, S. M., Huang, Y., and Seinfeld, J. H.: Computational Simulation of Secondary Organic Aerosol  
1032 Formation in Laboratory Chambers, *Chemical Reviews*, 119, 11912-11944,  
1033 10.1021/acs.chemrev.9b00358, 2019.

1034 Chen, H., Duan, F., Du, J., Yin, R., Zhu, L., Dong, J., He, K., Sun, Z., and Wang, S.: Surface-enhanced  
1035 Raman scattering for mixing state characterization of individual fine particles during a haze  
1036 episode in Beijing, China, *Journal of Environmental Sciences*, 104, 216-224,  
1037 <https://doi.org/10.1016/j.jes.2020.12.008>, 2021.

1038 Chen, X., Chu, Y., Lee, A. K., Gen, M., Kasthuriarachchi, N. Y., Chan, C. K., and Li, Y. J.: Relative  
1039 humidity history affects hygroscopicity of mixed particles of glyoxal and reduced nitrogenous  
1040 species, *Environmental science & technology*, 54, 7097-7106, 2020.

1041 Cheng, H., Dong, X., Yang, Y., Feng, Y., Wang, T., Tahir, M. A., Zhang, L., and Fu, H.: Au nanoring  
1042 arrays as surface enhanced Raman spectroscopy substrate for chemical component study of  
1043 individual atmospheric aerosol particle, *Journal of Environmental Sciences*, 100, 11-17,  
1044 <https://doi.org/10.1016/j.jes.2020.07.003>, 2021.

1045 Cheng, Y., Zheng, G., Wei, C., Mu, Q., Zheng, B., Wang, Z., Gao, M., Zhang, Q., He, K., Carmichael,  
1046 G., Pöschl, U., and Su, H.: Reactive nitrogen chemistry in aerosol water as a source of sulfate  
1047 during haze events in China, *Science Advances*, 2, e1601530, 10.1126/sciadv.1601530, 2016.

1048 Choi, M. Y., and Chan, C. K.: The Effects of Organic Species on the Hygroscopic Behaviors of Inorganic  
1049 Aerosols, *Environmental Science & Technology*, 36, 2422-2428, 10.1021/es0113293, 2002.

1050 Chu, Y., Sauerwein, M., and Chan, C. K.: Hygroscopic and phase transition properties of alkyl aminium  
1051 sulfates at low relative humidities, *Physical Chemistry Chemical Physics*, 17, 19789-19796,  
1052 2015.

1053 Chu, Y., and Chan, C. K.: Reactive Uptake of Dimethylamine by Ammonium Sulfate and Ammonium  
1054 Sulfate–Sucrose Mixed Particles, *The Journal of Physical Chemistry A*, 121, 206-215,  
1055 10.1021/acs.jpca.6b10692, 2017a.

1056 Chu, Y., and Chan, C. K.: Role of oleic acid coating in the heterogeneous uptake of dimethylamine by  
1057 ammonium sulfate particles, *Aerosol Science and Technology*, 51, 988-997,  
1058 10.1080/02786826.2017.1323072, 2017b.

1059 Chu, Y., Cheng, T. F., Gen, M., Chan, C. K., Lee, A. K. Y., and Chan, M. N.: Effect of Ozone  
1060 Concentration and Relative Humidity on the Heterogeneous Oxidation of Linoleic Acid  
1061 Particles by Ozone: An Insight into the Interchangeability of Ozone Concentration and Time,  
1062 *ACS Earth and Space Chemistry*, 3, 779-788, 10.1021/acsearthspacechem.9b00002, 2019.

1063 Ciavatta, L.: The specific interaction theory in evaluating ionic equilibria, *Ann. Chim.(Rome)*, 70, 551,  
1064 1980.

1065 Coddens, E. M., Angle, K. J., and Grassian, V. H.: Titration of Aerosol pH through Droplet Coalescence,  
1066 *J Phys Chem Lett*, 10, 4476-4483, 10.1021/acs.jpcllett.9b00757, 2019.

1067 Cohen, L., Quant, M. I., and Donaldson, D. J.: Real-Time Measurements of pH Changes in Single,

1068 Acoustically Levitated Droplets Due to Atmospheric Multiphase Chemistry, *ACS Earth and*  
1069 *Space Chemistry*, 4, 854-861, 10.1021/acsearthspacechem.0c00041, 2020.

1070 Collins, D. B., Hems, R. F., Zhou, S., Wang, C., Grignon, E., Alavy, M., Siegel, J. A., and Abbatt, J. P.  
1071 D.: Evidence for Gas-Surface Equilibrium Control of Indoor Nitrous Acid, *Environ Sci Technol*,  
1072 52, 12419-12427, 10.1021/acs.est.8b04512, 2018.

1073 Cotterell, M. I., Mason, B. J., Carruthers, A. E., Walker, J. S., Orr-Ewing, A. J., and Reid, J. P.:  
1074 Measurements of the evaporation and hygroscopic response of single fine-mode aerosol  
1075 particles using a Bessel beam optical trap, *Physical Chemistry Chemical Physics*, 16, 2118-2128,  
1076 2014.

1077 Craig, R. L., Bondy, A. L., and Ault, A. P.: Surface Enhanced Raman Spectroscopy Enables Observations  
1078 of Previously Undetectable Secondary Organic Aerosol Components at the Individual Particle  
1079 Level, *Analytical Chemistry*, 87, 7510-7514, 10.1021/acs.analchem.5b01507, 2015.

1080 Craig, R. L., Nandy, L., Axson, J. L., Dutcher, C. S., and Ault, A. P.: Spectroscopic Determination of  
1081 Aerosol pH from Acid-Base Equilibria in Inorganic, Organic, and Mixed Systems, *The Journal*  
1082 *of Physical Chemistry A*, 121, 5690-5699, 10.1021/acs.jpca.7b05261, 2017.

1083 Craig, R. L., Peterson, P. K., Nandy, L., Lei, Z., Hossain, M. A., Camarena, S., Dodson, R. A., Cook, R.  
1084 D., Dutcher, C. S., and Ault, A. P.: Direct Determination of Aerosol pH: Size-Resolved  
1085 Measurements of Submicrometer and Supermicrometer Aqueous Particles, *Analytical*  
1086 *Chemistry*, 90, 11232-11239, 10.1021/acs.analchem.8b00586, 2018.

1087 Cruz, C. N., and Pandis, S. N.: Deliquescence and Hygroscopic Growth of Mixed Inorganic-Organic  
1088 Atmospheric Aerosol, *Environmental Science & Technology*, 34, 4313-4319,  
1089 10.1021/es9907109, 2000.

1090 Cui, X., Tang, M., Wang, M., and Zhu, T.: Water as a probe for pH measurement in individual particles  
1091 using micro-Raman spectroscopy, *Analytica Chimica Acta*, 1186, 339089,  
1092 <https://doi.org/10.1016/j.aca.2021.339089>, 2021.

1093 Czamara, K., Majzner, K., Pacia, M. Z., Kochan, K., Kaczor, A., and Baranska, M.: Raman spectroscopy  
1094 of lipids: a review, *Journal of Raman Spectroscopy*, 46, 4-20, 2015.

1095 Davies, J. F., Haddrell, A. E., Rickards, A. M. J., and Reid, J. P.: Simultaneous Analysis of the  
1096 Equilibrium Hygroscopicity and Water Transport Kinetics of Liquid Aerosol, *Analytical*  
1097 *Chemistry*, 85, 5819-5826, 10.1021/ac4005502, 2013.

1098 Davies, J. F., and Wilson, K. R.: Raman Spectroscopy of Isotopic Water Diffusion in Ultraviscous, Glassy,  
1099 and Gel States in Aerosol by Use of Optical Tweezers, *Analytical Chemistry*, 88, 2361-2366,  
1100 10.1021/acs.analchem.5b04315, 2016.

1101 Davies, J. F.: Mass, charge, and radius of droplets in a linear quadrupole electrodynamic balance, *Aerosol*  
1102 *Science and Technology*, 53, 309-320, 10.1080/02786826.2018.1559921, 2019.

1103 Davis, E. J., and Ray, A.: Single aerosol particle size and mass measurements using an electrodynamic  
1104 balance, *Journal of Colloid and Interface Science*, 75, 566-576, 1980.

1105 Dennis-Smith, B. J., Hanford, K. L., Kwamena, N.-O. A., Miles, R. E. H., and Reid, J. P.: Phase,  
1106 Morphology, and Hygroscopicity of Mixed Oleic Acid/Sodium Chloride/Water Aerosol  
1107 Particles before and after Ozonolysis, *The Journal of Physical Chemistry A*, 116, 6159-6168,  
1108 10.1021/jp211429f, 2012.

1109 Duporté, G., Riva, M., Parshintsev, J., Heikkinen, E., Barreira, L. M. F., Myllys, N., Heikkinen, L.,  
1110 Hartonen, K., Kulmala, M., Ehn, M., and Riekkola, M.-L.: Chemical Characterization of Gas-  
1111 and Particle-Phase Products from the Ozonolysis of  $\alpha$ -Pinene in the Presence of Dimethylamine,

1112 Environmental Science & Technology, 51, 5602-5610, 10.1021/acs.est.6b06231, 2017.

1113 Efremov, E. V., Ariese, F., and Gooijer, C.: Achievements in resonance Raman spectroscopy: Review of  
1114 a technique with a distinct analytical chemistry potential, *Analytica chimica acta*, 606, 119-134,  
1115 2008.

1116 Enami, S., and Colussi, A. J.: Criegee Chemistry on Aqueous Organic Surfaces, *The Journal of Physical  
1117 Chemistry Letters*, 8, 1615-1623, 10.1021/acs.jpcelett.7b00434, 2017.

1118 Eom, H.-J., Gupta, D., Cho, H.-R., Hwang, H. J., Hur, S. D., Gim, Y., and Ro, C.-U.: Single-particle  
1119 investigation of summertime and wintertime Antarctic sea spray aerosols using low-Z particle  
1120 EPMA, Raman microspectrometry, and ATR-FTIR imaging techniques, *Atmospheric  
1121 Chemistry and Physics*, 16, 13823-13836, 2016.

1122 Falgayrac, G., Siepka, D., Stefaniak, E. A., Penel, G., and Sobanska, S.: Influence of collecting substrate  
1123 on the Raman imaging of micron-sized particles, *Analytica Chimica Acta*, 1014, 41-49,  
1124 <https://doi.org/10.1016/j.aca.2018.02.015>, 2018.

1125 Félix-Rivera, H., and Hernández-Rivera, S. P.: Raman Spectroscopy Techniques for the Detection of  
1126 Biological Samples in Suspensions and as Aerosol Particles: A Review, *Sensing and Imaging:  
1127 An International Journal*, 13, 1-25, 10.1007/s11220-011-0067-0, 2012.

1128 Fu, Y., Kuppe, C., Valev, V. K., Fu, H., Zhang, L., and Chen, J.: Surface-Enhanced Raman Spectroscopy:  
1129 A Facile and Rapid Method for the Chemical Component Study of Individual Atmospheric  
1130 Aerosol, *Environmental Science & Technology*, 51, 6260-6267, 10.1021/acs.est.6b05910, 2017.

1131 Gen, M., and Chan, C. K.: Electro spray surface-enhanced Raman spectroscopy (ES-SERS) for probing  
1132 surface chemical compositions of atmospherically relevant particles, *Atmospheric Chemistry &  
1133 Physics*, 17, 2017.

1134 Gen, M., Huang, D. D., and Chan, C. K.: Reactive Uptake of Glyoxal by Ammonium-Containing Salt  
1135 Particles as a Function of Relative Humidity, *Environ Sci Technol*, 52, 6903-6911,  
1136 10.1021/acs.est.8b00606, 2018a.

1137 Gen, M., Huang, D. D., and Chan, C. K.: Reactive uptake of glyoxal by ammonium-containing salt  
1138 particles as a function of relative humidity, *Environmental science & technology*, 52, 6903-6911,  
1139 2018b.

1140 Gen, M., Kunihisa, R., Matsuki, A., and Chan, C. K.: Electro spray surface-enhanced Raman  
1141 spectroscopy (ES-SERS) for studying organic coatings of atmospheric aerosol particles,  
1142 *Aerosol Science and Technology*, 53, 760-770, 10.1080/02786826.2019.1597964, 2019a.

1143 Gen, M., Zhang, R., Huang, D. D., Li, Y., and Chan, C. K.: Heterogeneous SO<sub>2</sub> Oxidation in Sulfate  
1144 Formation by Photolysis of Particulate Nitrate, *Environmental Science & Technology Letters*,  
1145 6, 86-91, 10.1021/acs.estlett.8b00681, 2019b.

1146 Gen, M., Zhang, R., Huang, D. D., Li, Y., and Chan, C. K.: Heterogeneous Oxidation of SO<sub>2</sub> in Sulfate  
1147 Production during Nitrate Photolysis at 300 nm: Effect of pH, Relative Humidity, Irradiation  
1148 Intensity, and the Presence of Organic Compounds, *Environ Sci Technol*, 53, 8757-8766,  
1149 10.1021/acs.est.9b01623, 2019c.

1150 Gen, M., Zhang, R., Li, Y., and Chan, C. K.: Multiphase Photochemistry of Iron-Chloride Containing  
1151 Particles as a Source of Aqueous Chlorine Radicals and Its Effect on Sulfate Production,  
1152 *Environmental Science & Technology*, 54, 9862-9871, 10.1021/acs.est.0c01540, 2020.

1153 George, I. J., and Abbatt, J. P.: Heterogeneous oxidation of atmospheric aerosol particles by gas-phase  
1154 radicals, *Nat Chem*, 2, 713-722, 10.1038/nchem.806, 2010.

1155 Ghosal, S., and Wall, S.: Identifying regional soil as the potential source of PM<sub>2.5</sub> particulate matter on

1156 air filters collected in Imperial Valley, California – A Raman micro-spectroscopy study,  
1157 Environmental Pollution, 253, 181-189, <https://doi.org/10.1016/j.envpol.2019.07.004>, 2019.

1158 Gómez Castaño, J. A., Boussekey, L., Verwaerde, J. P., Moreau, M., and Tobón, Y. A.: Enhancing Double-  
1159 Beam Laser Tweezers Raman Spectroscopy (LTRS) for the Photochemical Study of Individual  
1160 Airborne Microdroplets, *Molecules*, 24, 3325, 2019.

1161 Gong, Z., Pan, Y.-L., Videen, G., and Wang, C.: The temporal evolution process from fluorescence  
1162 bleaching to clean Raman spectra of single solid particles optically trapped in air, *Chemical  
1163 Physics Letters*, 689, 100-104, <https://doi.org/10.1016/j.cplett.2017.09.064>, 2017.

1164 Gong, Z., Pan, Y.-L., Videen, G., and Wang, C.: Optical trapping and manipulation of single particles in  
1165 air: Principles, technical details, and applications, *Journal of Quantitative Spectroscopy and  
1166 Radiative Transfer*, 214, 94-119, <https://doi.org/10.1016/j.jqsrt.2018.04.027>, 2018a.

1167 Gong, Z., Pan, Y.-L., Videen, G., and Wang, C.: Optical trapping-Raman spectroscopy (OT-RS) with  
1168 embedded microscopy imaging for concurrent characterization and monitoring of physical and  
1169 chemical properties of single particles, *Analytica Chimica Acta*, 1020, 86-94, 2018b.

1170 Gong, Z., Pan, Y.-L., Videen, G., and Wang, C.: Chemical reactions of single optically trapped  
1171 bioaerosols in a controlled environment, *Aerosol Science and Technology*, 53, 853-859,  
1172 10.1080/02786826.2019.1621984, 2019.

1173 Gorkowski, K., Donahue, N. M., and Sullivan, R. C.: Emulsified and Liquid-Liquid Phase-Separated  
1174 States of  $\alpha$ -Pinene Secondary Organic Aerosol Determined Using Aerosol Optical Tweezers,  
1175 *Environmental Science & Technology*, 51, 12154-12163, 10.1021/acs.est.7b03250, 2017.

1176 Gorkowski, K., Donahue, N. M., and Sullivan, R. C.: Aerosol Optical Tweezers Constrain the  
1177 Morphology Evolution of Liquid-Liquid Phase-Separated Atmospheric Particles, *Chem*, 6, 204-  
1178 220, <https://doi.org/10.1016/j.chempr.2019.10.018>, 2020.

1179 Heine, N., Arata, C., Goldstein, A. H., Houle, F. A., and Wilson, K. R.: Multiphase Mechanism for the  
1180 Production of Sulfuric Acid from SO<sub>2</sub> by Criegee Intermediates Formed During the  
1181 Heterogeneous Reaction of Ozone with Squalene, *The Journal of Physical Chemistry Letters*,  
1182 9, 3504-3510, 10.1021/acs.jpcl.8b01171, 2018.

1183 Huang, Q., Wei, H., Marr, L. C., and Vikesland, P. J.: Direct Quantification of the Effect of Ammonium  
1184 on Aerosol Droplet pH, *Environmental Science & Technology*, 10.1021/acs.est.0c07394, 2020.

1185 Huang, Y., Mahrt, F., Xu, S., Shiraiwa, M., Zuend, A., and Bertram, A. K.: Coexistence of three liquid  
1186 phases in individual atmospheric aerosol particles, *Proceedings of the National Academy of  
1187 Sciences*, 118, e2102512118, 10.1073/pnas.2102512118, 2021.

1188 Huffman, J. A., Perring, A. E., Savage, N. J., Clot, B., Crouzy, B., Tummon, F., Shoshanim, O., Damit,  
1189 B., Schneider, J., Sivaprakasam, V., Zawadowicz, M. A., Crawford, I., Gallagher, M., Topping,  
1190 D., Doughty, D. C., Hill, S. C., and Pan, Y.: Real-time sensing of bioaerosols: Review and  
1191 current perspectives, *Aerosol Science and Technology*, 54, 465-495,  
1192 10.1080/02786826.2019.1664724, 2020.

1193 Ishizaka, S., Yamamoto, C., and Yamagishi, H.: Liquid-Liquid Phase Separation of Single Optically  
1194 Levitated Water-Ionic Liquid Droplets in Air, *The Journal of Physical Chemistry A*, 125, 7716-  
1195 7722, 10.1021/acs.jpca.1c06130, 2021.

1196 Ivleva, N. P., McKeon, U., Niessner, R., and Pöschl, U.: Raman Microspectroscopic Analysis of Size-  
1197 Resolved Atmospheric Aerosol Particle Samples Collected with an ELPI: Soot, Humic-Like  
1198 Substances, and Inorganic Compounds, *Aerosol Science and Technology*, 41, 655-671,  
1199 10.1080/02786820701376391, 2007a.

1200 Ivleva, N. P., Messerer, A., Yang, X., Niessner, R., and Pöschl, U.: Raman Microspectroscopic Analysis  
1201 of Changes in the Chemical Structure and Reactivity of Soot in a Diesel Exhaust Aftertreatment  
1202 Model System, *Environmental Science & Technology*, 41, 3702-3707, 10.1021/es0612448,  
1203 2007b.

1204 Jacobs, M. I., Davies, J. F., Lee, L., Davis, R. D., Houle, F., and Wilson, K. R.: Exploring Chemistry in  
1205 Microcompartments Using Guided Droplet Collisions in a Branched Quadrupole Trap Coupled  
1206 to a Single Droplet, Paper Spray Mass Spectrometer, *Analytical Chemistry*, 89, 12511-12519,  
1207 10.1021/acs.analchem.7b03704, 2017.

1208 Jarvis, R. M., Law, N., Shadi, I. T., O'Brien, P., Lloyd, J. R., and Goodacre, R.: Surface-Enhanced Raman  
1209 Scattering from Intracellular and Extracellular Bacterial Locations, *Analytical Chemistry*, 80,  
1210 6741-6746, 10.1021/ac800838v, 2008.

1211 Jones, R. R., Hooper, D. C., Zhang, L., Wolverson, D., and Valev, V. K.: Raman techniques:  
1212 Fundamentals and frontiers, *Nanoscale research letters*, 14, 1-34, 2019.

1213 Jones, S. H., Friederich, P., and Donaldson, D. J.: Photochemical Aging of Levitated Aqueous Brown  
1214 Carbon Droplets, *ACS Earth and Space Chemistry*, 5, 749-754,  
1215 10.1021/acsearthspacechem.1c00005, 2021.

1216 Kalume, A., Beresnev, L. A., Santarpia, J., and Pan, Y.-L.: Detection and characterization of chemical  
1217 aerosol using laser-trapping single-particle Raman spectroscopy, *Appl. Opt.*, 56, 6577-6582,  
1218 10.1364/AO.56.006577, 2017a.

1219 Kalume, A., Zhu, E., Wang, C., Santarpia, J., and Pan, Y.-L.: Position-resolved Raman spectra from a  
1220 laser-trapped single airborne chemical droplet, *Opt. Lett.*, 42, 5113-5116,  
1221 10.1364/OL.42.005113, 2017b.

1222 Kalume, A., Wang, C., Santarpia, J., and Pan, Y.-L.: Liquid-liquid phase separation and evaporation of  
1223 a laser-trapped organic-organic airborne droplet using temporal spatial-resolved Raman  
1224 spectroscopy, *Physical Chemistry Chemical Physics*, 20, 19151-19159, 10.1039/C8CP02372G,  
1225 2018.

1226 Kampf, C. J., Liu, F., Reinmuth-Selzle, K., Berkemeier, T., Meusel, H., Shiraiwa, M., and Pöschl, U.:  
1227 Protein Cross-Linking and Oligomerization through Dityrosine Formation upon Exposure to  
1228 Ozone, *Environmental Science & Technology*, 49, 10859-10866, 10.1021/acs.est.5b02902,  
1229 2015.

1230 Kang, E., Root, M. J., Toohey, D. W., and Brune, W. H.: Introducing the concept of Potential Aerosol  
1231 Mass (PAM), *Atmos. Chem. Phys.*, 7, 5727-5744, 10.5194/acp-7-5727-2007, 2007.

1232 Keller, A., and Burtscher, H.: A continuous photo-oxidation flow reactor for a defined measurement of  
1233 the SOA formation potential of wood burning emissions, *Journal of aerosol science*, 49, 9-20,  
1234 2012.

1235 Kerminen, V.-M., Chen, X., Vakkari, V., Petäjä, T., Kulmala, M., and Bianchi, F.: Atmospheric new  
1236 particle formation and growth: review of field observations, *Environmental Research Letters*,  
1237 13, 103003, 2018.

1238 King, M. D., Thompson, K. C., and Ward, A. D.: Laser tweezers Raman study of optically trapped aerosol  
1239 droplets of seawater and oleic acid reacting with ozone: implications for cloud-droplet  
1240 properties, *Journal of the American chemical society*, 126, 16710-16711, 2004.

1241 King, M. D., Thompson, K. C., Ward, A. D., Pfrang, C., and Hughes, B. R.: Oxidation of biogenic and  
1242 water-soluble compounds in aqueous and organic aerosol droplets by ozone: a kinetic and  
1243 product analysis approach using laser Raman tweezers, *Faraday Discussions*, 137, 173-192,

1244 10.1039/B702199B, 2008.

1245 Kirkby, J., Curtius, J., Almeida, J., Dunne, E., Duplissy, J., Ehrhart, S., Franchin, A., Gagné, S., Ickes,  
1246 L., and Kürten, A.: Role of sulphuric acid, ammonia and galactic cosmic rays in atmospheric  
1247 aerosol nucleation, *Nature*, 476, 429-433, 2011.

1248 Kline, N. J., and Treado, P. J.: Raman chemical imaging of breast tissue, *Journal of Raman Spectroscopy*,  
1249 28, 119-124, 1997.

1250 Knopf, D., Koop, T., Luo, B., Weers, U., and Peter, T.: Homogeneous nucleation of NAD and NAT in  
1251 liquid stratospheric aerosols: insufficient to explain denitrification, 2002.

1252 Knopf, D. A., Luo, B. P., Krieger, U. K., and Koop, T.: Thermodynamic Dissociation Constant of the  
1253 Bisulfate Ion from Raman and Ion Interaction Modeling Studies of Aqueous Sulfuric Acid at  
1254 Low Temperatures, *The Journal of Physical Chemistry A*, 107, 4322-4332, 10.1021/jp027775+,  
1255 2003.

1256 Kohli, R. K., and Davies, J. F.: Measuring the Chemical Evolution of Levitated Particles: A Study on the  
1257 Evaporation of Multicomponent Organic Aerosol, *Analytical Chemistry*, 93, 12472-12479,  
1258 2021.

1259 Krieger, U. K., Marcolli, C., and Reid, J. P.: Exploring the complexity of aerosol particle properties and  
1260 processes using single particle techniques, *Chemical Society Reviews*, 41, 6631-6662, 2012.

1261 Kuniyama, R., Iwata, A., Gen, M., Chan, C. K., and Matsuki, A.: Application of SERS on the chemical  
1262 speciation of individual Aitken mode particles after condensational growth, *Aerosol Science  
1263 and Technology*, 54, 826-836, 10.1080/02786826.2020.1730298, 2020.

1264 Kuwata, M., and Martin, S. T.: Phase of atmospheric secondary organic material affects its reactivity,  
1265 *Proc Natl Acad Sci U S A*, 109, 17354-17359, 10.1073/pnas.1209071109, 2012.

1266 Kwamena, N. O. A., Buajarnern, J., and Reid, J. P.: Equilibrium Morphology of Mixed  
1267 Organic/Inorganic/Aqueous Aerosol Droplets: Investigating the Effect of Relative Humidity  
1268 and Surfactants, *The Journal of Physical Chemistry A*, 114, 5787-5795, 10.1021/jp1003648,  
1269 2010.

1270 Lam, H. K., Xu, R., Choczynski, J., Davies, J. F., Ham, D., Song, M., Zuend, A., Li, W., Tse, Y. L. S.,  
1271 and Chan, M. N.: Effects of liquid-liquid phase separation and relative humidity on the  
1272 heterogeneous OH oxidation of inorganic-organic aerosols: insights from methylglutaric acid  
1273 and ammonium sulfate particles, *Atmos. Chem. Phys.*, 21, 2053-2066, 10.5194/acp-21-2053-  
1274 2021, 2021.

1275 Laskin, A., Laskin, J., and Nizkorodov, S. A.: Chemistry of atmospheric brown carbon, *Chem Rev*, 115,  
1276 4335-4382, 10.1021/cr5006167, 2015.

1277 Laskina, O., Young, M. A., Kleiber, P. D., and Grassian, V. H.: Infrared extinction spectroscopy and  
1278 micro-Raman spectroscopy of select components of mineral dust mixed with organic  
1279 compounds, *Journal of Geophysical Research: Atmospheres*, 118, 6593-6606,  
1280 <https://doi.org/10.1002/jgrd.50494>, 2013.

1281 Laskina, O., Morris, H. S., Grandquist, J. R., Qin, Z., Stone, E. A., Tivanski, A. V., and Grassian, V. H.:  
1282 Size Matters in the Water Uptake and Hygroscopic Growth of Atmospherically Relevant  
1283 Multicomponent Aerosol Particles, *The Journal of Physical Chemistry A*, 119, 4489-4497,  
1284 10.1021/jp510268p, 2015.

1285 Laucks, M. L., Roll, G., Schweiger, G., and Davis, E. J.: PHYSICAL AND CHEMICAL (RAMAN)  
1286 CHARACTERIZATION OF BIOAEROSOLS—POLLEN, *Journal of Aerosol Science*, 31,  
1287 307-319, [https://doi.org/10.1016/S0021-8502\(99\)00058-0](https://doi.org/10.1016/S0021-8502(99)00058-0), 2000.

1288 Lee, A. K., Ling, T., and Chan, C. K.: Understanding hygroscopic growth and phase transformation of  
1289 aerosols using single particle Raman spectroscopy in an electrodynamic balance, *Faraday*  
1290 *Discussions*, 137, 245-263, 2008a.

1291 Lee, A. K. Y., and Chan, C. K.: Single particle Raman spectroscopy for investigating atmospheric  
1292 heterogeneous reactions of organic aerosols, *Atmospheric Environment*, 41, 4611-4621,  
1293 <https://doi.org/10.1016/j.atmosenv.2007.03.040>, 2007a.

1294 Lee, A. K. Y., and Chan, C. K.: Heterogeneous Reactions of Linoleic Acid and Linolenic Acid Particles  
1295 with Ozone: Reaction Pathways and Changes in Particle Mass, Hygroscopicity, and  
1296 Morphology, *The Journal of Physical Chemistry A*, 111, 6285-6295, 10.1021/jp071812l, 2007b.

1297 Lee, A. K. Y., Li, Y. J., Lau, A. P. S., and Chan, C. K.: A Re-Evaluation on the Atmospheric Significance  
1298 of Octanal Vapor Uptake by Acidic Particles: Roles of Particle Acidity and Gas-Phase Octanal  
1299 Concentration, *Aerosol Science and Technology*, 42, 992-1000, 10.1080/02786820802382736,  
1300 2008b.

1301 Lee, J. S., Ahn, Y., Kim, J., Kim, J., Nam, S. H., Yu, S.-C., Shin, H. H., Jung, T., Kim, E.-A., Suh, Y. D.,  
1302 Kim, H. W., and Park, H.-R.: Chemical analysis of air pollutant particulate matters based on  
1303 surface enhanced Raman spectroscopy (SERS), *SPIE Nanoscience + Engineering*, SPIE, 2019.

1304 Li, J. F., Huang, Y. F., Ding, Y., Yang, Z. L., Li, S. B., Zhou, X. S., Fan, F. R., Zhang, W., Zhou, Z. Y.,  
1305 Wu, D. Y., Ren, B., Wang, Z. L., and Tian, Z. Q.: Shell-isolated nanoparticle-enhanced Raman  
1306 spectroscopy, *Nature*, 464, 392-395, 10.1038/nature08907, 2010.

1307 Li, R., Palm, B. B., Ortega, A. M., Hlywiak, J., Hu, W., Peng, Z., Day, D. A., Knote, C., Brune, W. H.,  
1308 de Gouw, J. A., and Jimenez, J. L.: Modeling the Radical Chemistry in an Oxidation Flow  
1309 Reactor: Radical Formation and Recycling, Sensitivities, and the OH Exposure Estimation  
1310 Equation, *The Journal of Physical Chemistry A*, 119, 4418-4432, 10.1021/jp509534k, 2015.

1311 Li, X., Gupta, D., Lee, J., Park, G., and Ro, C.-U.: Real-Time Investigation of Chemical Compositions  
1312 and Hygroscopic Properties of Aerosols Generated from NaCl and Malonic Acid Mixture  
1313 Solutions Using in Situ Raman Microspectrometry, *Environmental Science & Technology*, 51,  
1314 263-270, 10.1021/acs.est.6b04356, 2017.

1315 Li, X., Wu, L., Lee, J.-S., and Ro, C.-U.: Hygroscopic behavior and chemical reactivity of aerosols  
1316 generated from mixture solutions of low molecular weight dicarboxylic acids and NaCl,  
1317 *Physical Chemistry Chemical Physics*, 23, 11052-11064, 2021.

1318 Li, Y. J., Lee, A. K., Lau, A. P., and Chan, C. K.: Accretion reactions of octanal catalyzed by sulfuric acid:  
1319 Product identification, reaction pathways, and atmospheric implications, *Environmental science*  
1320 *& technology*, 42, 7138-7145, 2008.

1321 Liang, Z., Zhang, R., Gen, M., Chu, Y., and Chan, C. K.: Nitrate Photolysis in Mixed Sucrose–Nitrate–  
1322 Sulfate Particles at Different Relative Humidities, *The Journal of Physical Chemistry A*,  
1323 10.1021/acs.jpca.1c00669, 2021.

1324 Ling, T. Y., and Chan, C. K.: Formation and Transformation of Metastable Double Salts from the  
1325 Crystallization of Mixed Ammonium Nitrate and Ammonium Sulfate Particles, *Environmental*  
1326 *Science & Technology*, 41, 8077-8083, 10.1021/es071419t, 2007.

1327 Ling, T. Y., and Chan, C. K.: Partial crystallization and deliquescence of particles containing ammonium  
1328 sulfate and dicarboxylic acids, *Journal of Geophysical Research: Atmospheres*, 113,  
1329 <https://doi.org/10.1029/2008JD009779>, 2008.

1330 Liu, T., Wang, X., Hu, Q., Deng, W., Zhang, Y., Ding, X., Fu, X., Bernard, F., Zhang, Z., Lü, S., He, Q.,  
1331 Bi, X., Chen, J., Sun, Y., Yu, J., Peng, P., Sheng, G., and Fu, J.: Formation of secondary aerosols



1332 from gasoline vehicle exhaust when mixing with SO<sub>2</sub>, *Atmos. Chem. Phys.*, 16, 675-689,  
1333 10.5194/acp-16-675-2016, 2016.

1334 Liu, T., and Abbatt, J. P.: An experimental assessment of the importance of S (IV) oxidation by  
1335 hypohalous acids in the marine atmosphere, *Geophysical Research Letters*, 47, e2019GL086465,  
1336 2020.

1337 Liu, T., Clegg, S. L., and Abbatt, J. P.: Fast oxidation of sulfur dioxide by hydrogen peroxide in  
1338 deliquesced aerosol particles, *Proceedings of the National Academy of Sciences*, 117, 1354-  
1339 1359, 2020a.

1340 Liu, T., and Abbatt, J. P. D.: Oxidation of sulfur dioxide by nitrogen dioxide accelerated at the interface  
1341 of deliquesced aerosol particles, *Nature Chemistry*, 13, 1173-1177, 10.1038/s41557-021-00777-  
1342 0, 2021.

1343 Liu, T., Chan, A. W. H., and Abbatt, J. P. D.: Multiphase Oxidation of Sulfur Dioxide in Aerosol Particles:  
1344 Implications for Sulfate Formation in Polluted Environments, *Environmental Science &  
1345 Technology*, 55, 4227-4242, 10.1021/acs.est.0c06496, 2021.

1346 Liu, X., Knauer, M., Ivleva, N. P., Niessner, R., and Haisch, C.: Synthesis of Core-Shell Surface-  
1347 Enhanced Raman Tags for Bioimaging, *Analytical Chemistry*, 82, 441-446, 10.1021/ac902573p,  
1348 2010.

1349 Liu, Y., Zhu, T., Zhao, D., and Zhang, Z.: Investigation of the hygroscopic properties of Ca (NO<sub>3</sub>)<sub>2</sub> and  
1350 internally mixed Ca (NO<sub>3</sub>)<sub>2</sub>/CaCO<sub>3</sub> particles by micro-Raman spectrometry, 2008.

1351 Liu, Y., Zhou, H., Hu, Z., Yu, G., Yang, D., and Zhao, J.: Label and label-free based surface-enhanced  
1352 Raman scattering for pathogen bacteria detection: A review, *Biosensors and Bioelectronics*, 94,  
1353 131-140, <https://doi.org/10.1016/j.bios.2017.02.032>, 2017.

1354 Liu, Y., Wang, T., Fang, X., Deng, Y., Cheng, H., Bacha, A.-U.-R., Nabi, I., and Zhang, L.: Brown carbon:  
1355 An underlying driving force for rapid atmospheric sulfate formation and haze event, *Science of  
1356 The Total Environment*, 734, 139415, <https://doi.org/10.1016/j.scitotenv.2020.139415>, 2020b.

1357 Lu, J. W., Isenor, M., Chasovskikh, E., Stapfer, D., and Signorell, R.: Low-temperature Bessel beam trap  
1358 for single submicrometer aerosol particle studies, *Review of Scientific Instruments*, 85, 095107,  
1359 2014.

1360 Ma, Q., Liu, C., Ma, J., Chu, B., and He, H.: A laboratory study on the hygroscopic behavior of H<sub>2</sub>C<sub>2</sub>O<sub>4</sub>-  
1361 containing mixed particles, *Atmospheric Environment*, 200, 34-39,  
1362 <https://doi.org/10.1016/j.atmosenv.2018.11.056>, 2019a.

1363 Ma, Q., Zhong, C., Liu, C., Liu, J., Ma, J., Wu, L., and He, H.: A Comprehensive Study about the  
1364 Hygroscopic Behavior of Mixtures of Oxalic Acid and Nitrate Salts: Implication for the  
1365 Occurrence of Atmospheric Metal Oxalate Complex, *ACS Earth and Space Chemistry*, 3, 1216-  
1366 1225, 10.1021/acsearthspacechem.9b00077, 2019b.

1367 Ma, S., Chen, Z., Pang, S., and Zhang, Y.: Observations on hygroscopic growth and phase transitions of  
1368 mixed 1, 2, 6-hexanetriol&thinsp;&thinsp;(NH<sub>4</sub>)<sub>2</sub>SO<sub>4</sub> particles: investigation of the liquid-  
1369 liquid phase separation (LLPS) dynamic process and mechanism and secondary LLPS during  
1370 the dehumidification, *Atmos. Chem. Phys.*, 21, 9705-9717, 10.5194/acp-21-9705-2021, 2021.

1371 Mabato, B. R. G., Gen, M., Chu, Y., and Chan, C. K.: Reactive Uptake of Glyoxal by Methylammonium-  
1372 Containing Salts as a Function of Relative Humidity, *ACS Earth and Space Chemistry*, 3, 150-  
1373 157, 10.1021/acsearthspacechem.8b00154, 2019.

1374 Mael, L. E., Busse, H., and Grassian, V. H.: Measurements of Immersion Freezing and Heterogeneous  
1375 Chemistry of Atmospherically Relevant Single Particles with Micro-Raman Spectroscopy,

1376 Analytical Chemistry, 91, 11138-11145, 10.1021/acs.analchem.9b01819, 2019.

1377 Mael, L. E., Busse, H. L., Peiker, G., and Grassian, V. H.: Low-Temperature Water Uptake of Individual  
1378 Marine and Biologically Relevant Atmospheric Particles Using Micro-Raman Spectroscopy,  
1379 The Journal of Physical Chemistry A, 125, 9691-9699, 10.1021/acs.jpca.1c08037, 2021.

1380 Marcolli, C., and Krieger, U. K.: Relevance of particle morphology for atmospheric aerosol processing,  
1381 Trends in Chemistry, 2, 1-3, 2020.

1382 Marsh, A., Miles, R. E. H., Rovelli, G., Cowling, A. G., Nandy, L., Dutcher, C. S., and Reid, J. P.:  
1383 Influence of organic compound functionality on aerosol hygroscopicity: dicarboxylic acids,  
1384 alkyl-substituents, sugars and amino acids, Atmos. Chem. Phys., 17, 5583-5599, 10.5194/acp-  
1385 17-5583-2017, 2017.

1386 Marsh, A., Rovelli, G., Miles, R. E. H., and Reid, J. P.: Complexity of Measuring and Representing the  
1387 Hygroscopicity of Mixed Component Aerosol, The Journal of Physical Chemistry A, 123, 1648-  
1388 1660, 10.1021/acs.jpca.8b11623, 2019.

1389 Mekic, M., Wang, Y., Loisel, G., Vione, D., and Gligorovski, S.: Ionic Strength Effect Alters the  
1390 Heterogeneous Ozone Oxidation of Methoxyphenols in Going from Cloud Droplets to Aerosol  
1391 Deliquescent Particles, Environmental Science & Technology, 54, 12898-12907,  
1392 10.1021/acs.est.0c03648, 2020.

1393 Meresman, H., Wills, J. B., Summers, M., McGloin, D., and Reid, J. P.: Manipulation and  
1394 characterisation of accumulation and coarse mode aerosol particles using a Bessel beam trap,  
1395 Physical Chemistry Chemical Physics, 11, 11333-11339, 2009.

1396 Mikhailov, E., Vlasenko, S., Martin, S. T., Koop, T., and Pöschl, U.: Amorphous and crystalline aerosol  
1397 particles interacting with water vapor: conceptual framework and experimental evidence for  
1398 restructuring, phase transitions and kinetic limitations, Atmos. Chem. Phys., 9, 9491-9522,  
1399 10.5194/acp-9-9491-2009, 2009.

1400 Miles, R. E. H., Walker, J. S., Burnham, D. R., and Reid, J. P.: Retrieval of the complex refractive index  
1401 of aerosol droplets from optical tweezers measurements, Physical Chemistry Chemical Physics,  
1402 14, 3037-3047, 10.1039/C2CP23999J, 2012.

1403 Milsom, A., Squires, A. M., Boswell, J. A., Terrill, N. J., Ward, A. D., and Pfrang, C.: An organic  
1404 crystalline state in ageing atmospheric aerosol proxies: spatially resolved structural changes in  
1405 levitated fatty acid particles, Atmos. Chem. Phys., 21, 15003-15021, 10.5194/acp-21-15003-  
1406 2021, 2021.

1407 Mitchem, L., Buajarern, J., Hopkins, R. J., Ward, A. D., Gilham, R. J. J., Johnston, R. L., and Reid, J. P.:  
1408 Spectroscopy of Growing and Evaporating Water Droplets: Exploring the Variation in  
1409 Equilibrium Droplet Size with Relative Humidity, The Journal of Physical Chemistry A, 110,  
1410 8116-8125, 10.1021/jp061135f, 2006.

1411 Mitchem, L., and Reid, J. P.: Optical manipulation and characterisation of aerosol particles using a single-  
1412 beam gradient force optical trap, Chemical Society Reviews, 37, 756-769, 10.1039/B609713H,  
1413 2008.

1414 Mosier-Boss, P. A.: Review on SERS of Bacteria, Biosensors, 7, 51, 2017.

1415 Movasaghi, Z., Rehman, S., and Rehman, I. U.: Raman Spectroscopy of Biological Tissues, Applied  
1416 Spectroscopy Reviews, 42, 493-541, 10.1080/05704920701551530, 2007.

1417 Nadler, K. A., Kim, P., Huang, D.-L., Xiong, W., and Continetti, R. E.: Water diffusion measurements of  
1418 single charged aerosols using H<sub>2</sub>O/D<sub>2</sub>O isotope exchange and Raman spectroscopy in an  
1419 electrodynamic balance, Physical Chemistry Chemical Physics, 21, 15062-15071,

1420 10.1039/C8CP07052K, 2019.

1421 Nakajima, R., Miura, A., Abe, S., and Kitamura, N.: Optical Trapping–Polarized Raman  
1422 Microspectroscopy of Single Ethanol Aerosol Microdroplets: Droplet Size Effects on Rotational  
1423 Relaxation Time and Viscosity, *Analytical Chemistry*, 93, 5218-5224,  
1424 10.1021/acs.analchem.0c05406, 2021.

1425 Nishikida, K., Nishio, E., and Hannah, R. W.: Selected applications of modern FT-IR techniques,  
1426 Routledge, 2018.

1427 Offroy, M., Moreau, M., Sobanska, S., Milanfar, P., and Duponchel, L.: Pushing back the limits of Raman  
1428 imaging by coupling super-resolution and chemometrics for aerosols characterization,  
1429 *Scientific Reports*, 5, 12303, 10.1038/srep12303, 2015.

1430 Ofner, J., Deckert-Gaudig, T., Kamilli, K. A., Held, A., Lohninger, H., Deckert, V., and Lendl, B.: Tip-  
1431 Enhanced Raman Spectroscopy of Atmospherically Relevant Aerosol Nanoparticles, *Analytical*  
1432 *Chemistry*, 88, 9766-9772, 10.1021/acs.analchem.6b02760, 2016.

1433 Olson, N. E., Lei, Z., Craig, R. L., Zhang, Y., Chen, Y., Lambe, A. T., Zhang, Z., Gold, A., Surratt, J. D.,  
1434 and Ault, A. P.: Reactive Uptake of Isoprene Epoxydiols Increases the Viscosity of the Core of  
1435 Phase-Separated Aerosol Particles, *ACS Earth and Space Chemistry*, 3, 1402-1414,  
1436 10.1021/acsearthspacechem.9b00138, 2019.

1437 Pajunoja, A., Hu, W., Leong, Y. J., Taylor, N. F., Miettinen, P., Palm, B. B., Mikkonen, S., Collins, D. R.,  
1438 Jimenez, J. L., and Virtanen, A.: Phase state of ambient aerosol linked with water uptake and  
1439 chemical aging in the southeastern US, *Atmospheric Chemistry and Physics*, 16, 11163-11176,  
1440 2016.

1441 Pan, Y.-L., Hill, S. C., and Coleman, M.: Photophoretic trapping of absorbing particles in air and  
1442 measurement of their single-particle Raman spectra, *Opt. Express*, 20, 5325-5334,  
1443 10.1364/OE.20.005325, 2012.

1444 Parmentier, E. A., David, G., Arroyo, P. C., Bibawi, S., Esat, K., and Signorell, R.: Photochemistry of  
1445 single optically trapped oleic acid droplets, *Journal of Aerosol Science*, 151, 105660,  
1446 <https://doi.org/10.1016/j.jaerosci.2020.105660>, 2021.

1447 Parsons, M. T., Mak, J., Lipetz, S. R., and Bertram, A. K.: Deliquescence of malonic, succinic, glutaric,  
1448 and adipic acid particles, *Journal of Geophysical Research: Atmospheres*, 109,  
1449 <https://doi.org/10.1029/2003JD004075>, 2004.

1450 Peng, C., Chan, M. N., and Chan, C. K.: The Hygroscopic Properties of Dicarboxylic and Multifunctional  
1451 Acids: Measurements and UNIFAC Predictions, *Environmental Science & Technology*, 35,  
1452 4495-4501, 10.1021/es0107531, 2001.

1453 Peng, Z., and Jimenez, J. L.: Radical chemistry in oxidation flow reactors for atmospheric chemistry  
1454 research, *Chemical Society Reviews*, 49, 2570-2616, 10.1039/C9CS00766K, 2020.

1455 Pöschl, U.: *Atmospheric Aerosols: Composition, Transformation, Climate and Health Effects*,  
1456 *Angewandte Chemie International Edition*, 44, 7520-7540,  
1457 <https://doi.org/10.1002/anie.200501122>, 2005.

1458 Power, R., Simpson, S., Reid, J., and Hudson, A.: The transition from liquid to solid-like behaviour in  
1459 ultrahigh viscosity aerosol particles, *Chemical Science*, 4, 2597-2604, 2013.

1460 Price, C. L., Bain, A., Wallace, B. J., Preston, T. C., and Davies, J. F.: Simultaneous Retrieval of the Size  
1461 and Refractive Index of Suspended Droplets in a Linear Quadrupole Electrodynamic Balance,  
1462 *The Journal of Physical Chemistry A*, 124, 1811-1820, 10.1021/acs.jpca.9b10748, 2020.

1463 Qin, Y., Ye, J., Ohno, P., Zhai, J., Han, Y., Liu, P., Wang, J., Zaveri, R. A., and Martin, S. T.: Humidity

1464 Dependence of the Condensational Growth of  $\alpha$ -Pinene Secondary Organic Aerosol Particles,  
1465 Environmental Science & Technology, 55, 14360-14369, 10.1021/acs.est.1c01738, 2021.

1466 Qiu, J., Ishizuka, S., Tonokura, K., and Enami, S.: Interfacial vs Bulk Ozonolysis of Nerolidol,  
1467 Environmental Science & Technology, 53, 5750-5757, 10.1021/acs.est.9b00364, 2019.

1468 Qiu, J., Liang, Z., Tonokura, K., Colussi, A. J., and Enami, S.: Stability of Monoterpene-Derived  $\alpha$ -  
1469 Hydroxyalkyl-Hydroperoxides in Aqueous Organic Media: Relevance to the Fate of  
1470 Hydroperoxides in Aerosol Particle Phases, Environmental Science & Technology, 54, 3890-  
1471 3899, 10.1021/acs.est.9b07497, 2020.

1472 Radić, N., and Prkić, A.: Historical remarks on the Henderson-Hasselbalch equation: its advantages and  
1473 limitations and a novel approach for exact pH calculation in buffer region, Reviews in  
1474 Analytical Chemistry, 31, 93-98, 2012.

1475 Rafferty, A., and Preston, T. C.: Measuring the size and complex refractive index of an aqueous aerosol  
1476 particle using electromagnetic heating and cavity-enhanced Raman scattering, Physical  
1477 Chemistry Chemical Physics, 20, 17038-17047, 10.1039/C8CP02966K, 2018.

1478 Redding, B., Hill, S. C., Alexson, D., Wang, C., and Pan, Y.-L.: Photophoretic trapping of airborne  
1479 particles using ultraviolet illumination, Opt. Express, 23, 3630-3639, 10.1364/OE.23.003630,  
1480 2015a.

1481 Redding, B., and Pan, Y.-L.: Optical trap for both transparent and absorbing particles in air using a single  
1482 shaped laser beam, Opt. Lett., 40, 2798-2801, 10.1364/OL.40.002798, 2015.

1483 Redding, B., Schwab, M. J., and Pan, Y.-L.: Raman spectroscopy of optically trapped single biological  
1484 micro-particles, Sensors, 15, 19021-19046, 2015b.

1485 Reid, J. P., and Mitchem, L.: LASER PROBING OF SINGLE-AEROSOL DROPLET DYNAMICS,  
1486 Annual Review of Physical Chemistry, 57, 245-271,  
1487 10.1146/annurev.physchem.57.032905.104621, 2006.

1488 Renbaum-Wolff, L., Song, M., Marcolli, C., Zhang, Y., Liu, P. F., Grayson, J. W., Geiger, F. M., Martin,  
1489 S. T., and Bertram, A. K.: Observations and implications of liquid-liquid phase separation at  
1490 high relative humidities in secondary organic material produced by  $\alpha$ -pinene ozonolysis without  
1491 inorganic salts, Atmospheric Chemistry and Physics, 16, 7969-7979, 2016.

1492 Richards, D. S., Trobaugh, K. L., Hajek-Herrera, J., Price, C. L., Sheldon, C. S., Davies, J. F., and Davis,  
1493 R. D.: Ion-molecule interactions enable unexpected phase transitions in organic-inorganic  
1494 aerosol, Science Advances, 6, eabb5643, 10.1126/sciadv.abb5643, 2020.

1495 Rindelaub, J. D., Craig, R. L., Nandy, L., Bondy, A. L., Dutcher, C. S., Shepson, P. B., and Ault, A. P.:  
1496 Direct Measurement of pH in Individual Particles via Raman Microspectroscopy and Variation  
1497 in Acidity with Relative Humidity, The Journal of Physical Chemistry A, 120, 911-917,  
1498 10.1021/acs.jpca.5b12699, 2016.

1499 Rkiouak, L., Tang, M., Camp, J., McGregor, J., Watson, I., Cox, R., Kalberer, M., Ward, A., and Pope,  
1500 F.: Optical trapping and Raman spectroscopy of solid particles, Physical Chemistry Chemical  
1501 Physics, 16, 11426-11434, 2014.

1502 Rodriguez, R. D., Sheremet, E., Deckert-Gaudig, T., Chaneac, C., Hietschold, M., Deckert, V., and Zahn,  
1503 D. R. T.: Surface- and tip-enhanced Raman spectroscopy reveals spin-waves in iron oxide  
1504 nanoparticles, Nanoscale, 7, 9545-9551, 10.1039/C5NR01277E, 2015.

1505 Rosati, B., Paul, A., Iversen, E. M., Massling, A., and Bilde, M.: Reconciling atmospheric water uptake  
1506 by hydrate forming salts, Environmental Science: Processes & Impacts, 22, 1759-1767, 2020.

1507 Rovelli, G., Miles, R. E. H., Reid, J. P., and Clegg, S. L.: Accurate Measurements of Aerosol Hygroscopic

1508 Growth over a Wide Range in Relative Humidity, *The Journal of Physical Chemistry A*, 120,  
1509 4376-4388, 10.1021/acs.jpca.6b04194, 2016.

1510 Roy, P., Mael, L. E., Makhnenko, I., Martz, R., Grassian, V. H., and Dutcher, C. S.: Temperature-  
1511 Dependent Phase Transitions of Aqueous Aerosol Droplet Systems in Microfluidic Traps, *ACS*  
1512 *Earth and Space Chemistry*, 4, 1527-1539, 10.1021/acsearthspacechem.0c00114, 2020.

1513 Rygula, A., Majzner, K., Marzec, K. M., Kaczor, A., Pilarczyk, M., and Baranska, M.: Raman  
1514 spectroscopy of proteins: a review, *Journal of Raman Spectroscopy*, 44, 1061-1076, 2013.

1515 Sahoo, S. K., Umopathy, S., and Parker, A. W.: Time-Resolved Resonance Raman Spectroscopy:  
1516 Exploring Reactive Intermediates, *Applied Spectroscopy*, 65, 1087-1115, 2011.

1517 Saniel, M. B. B., Lim, L. H. V., and Lamorena, R. B.: An Initial Study on the Feasibility of Using  
1518 Rudimentary SERS in Quick Chemical Assessment of Ambient Aerosols, *ChemistrySelect*, 4,  
1519 14082-14090, <https://doi.org/10.1002/slct.201903479>, 2019.

1520 Sauerwein, M., and Chan, C. K.: Heterogeneous uptake of ammonia and dimethylamine into sulfuric and  
1521 oxalic acid particles, *Atmospheric Chemistry & Physics*, 17, 2017.

1522 Schill, G. P., De Haan, D. O., and Tolbert, M. A.: Heterogeneous Ice Nucleation on Simulated Secondary  
1523 Organic Aerosol, *Environmental Science & Technology*, 48, 1675-1682, 10.1021/es4046428,  
1524 2014.

1525 Scolaro, S., Sobanska, S., Barbillat, J., Laureyns, J., Louis, F., Petitprez, D., and Brémard, C.: Confocal  
1526 Raman imaging and atomic force microscopy of the surface reaction of NO<sub>2</sub> and NaCl (100)  
1527 under humidity, *Journal of Raman Spectroscopy: An International Journal for Original Work in*  
1528 *all Aspects of Raman Spectroscopy, Including Higher Order Processes, and also Brillouin and*  
1529 *Rayleigh Scattering*, 40, 157-163, 2009.

1530 Seinfeld, J. H., and Pandis, S. N.: *Atmospheric chemistry and physics: from air pollution to climate*  
1531 *change*, John Wiley & Sons, 2016.

1532 Seng, S., Guo, F., Tobon, Y. A., Ishikawa, T., Moreau, M., Ishizaka, S., and Sobanska, S.: Deliquescence  
1533 behavior of photo-irradiated single NaNO<sub>3</sub> droplets, *Atmospheric Environment*, 183, 33-39,  
1534 <https://doi.org/10.1016/j.atmosenv.2018.04.007>, 2018.

1535 Sengupta, A., Laucks, M. L., Dildine, N., Drapala, E., and Davis, E. J.: Bioaerosol characterization by  
1536 surface-enhanced Raman spectroscopy (SERS), *Journal of Aerosol Science*, 36, 651-664,  
1537 <https://doi.org/10.1016/j.jaerosci.2004.11.001>, 2005.

1538 Setschenow, J.: Über die Konstitution der Salzlösungen auf Grund ihres Verhaltens zu Kohlensäure,  
1539 *Zeitschrift für Physikalische Chemie*, 4U, 117, <https://doi.org/10.1515/zpch-1889-0409>, 1889.

1540 Singh, M., Mayya, Y. S., Gaware, J., and Thaokar, R. M.: Levitation dynamics of a collection of charged  
1541 droplets in an electrodynamic balance, *Journal of Applied Physics*, 121, 054503,  
1542 10.1063/1.4974470, 2017.

1543 Singh, M., Thaokar, R., Khan, A., and Mayya, Y. S.: Theoretical analysis of formation of many-drop  
1544 arrays in a quadrupole electrodynamic balance, *Physical Review E*, 98, 032202,  
1545 10.1103/PhysRevE.98.032202, 2018.

1546 Sivaprakasam, V., Hart, M. B., and Eversole, J. D.: Surface Enhanced Raman Spectroscopy of Individual  
1547 Suspended Aerosol Particles, *The Journal of Physical Chemistry C*, 121, 22326-22334,  
1548 10.1021/acs.jpcc.7b05310, 2017.

1549 Sivaprakasam, V., and Hart, M. B.: Surface-Enhanced Raman Spectroscopy for Environmental  
1550 Monitoring of Aerosols, *ACS Omega*, 10.1021/acsomega.1c00207, 2021.

1551 Smith, J., Kroll, J., Cappa, C., Che, D., Liu, C., Ahmed, M., Leone, S., Worsnop, D., and Wilson, K.: The

1552 heterogeneous reaction of hydroxyl radicals with sub-micron squalane particles: a model system  
1553 for understanding the oxidative aging of ambient aerosols, *Atmospheric Chemistry and Physics*,  
1554 9, 3209-3222, 2009.

1555 Sobanska, S., Falgayrac, G., Laureyns, J., and Brémard, C.: Chemistry at level of individual aerosol  
1556 particle using multivariate curve resolution of confocal Raman image, *Spectrochimica Acta Part*  
1557 *A: Molecular and Biomolecular Spectroscopy*, 64, 1102-1109,  
1558 <https://doi.org/10.1016/j.saa.2005.11.038>, 2006.

1559 Sobanska, S., Falgayrac, G., Rimetz-Planchon, J., Perdrix, E., Brémard, C., and Barbillat, J.: Resolving  
1560 the internal structure of individual atmospheric aerosol particle by the combination of Atomic  
1561 Force Microscopy, ESEM–EDX, Raman and ToF–SIMS imaging, *Microchemical Journal*, 114,  
1562 89-98, <https://doi.org/10.1016/j.microc.2013.12.007>, 2014.

1563 Sobanska, S., Dappe, V., Siepka, D., Moreau, M., Tobon, Y., and Stefaniak, E. A.: Automated Raman  
1564 microspectrometry and Raman imaging for atmospheric particle, *Euroanalysis 2015*, Bordeaux,  
1565 France, 2015-09, 2015.

1566 Socrates, G.: *Infrared and Raman characteristic group frequencies: tables and charts*, John Wiley & Sons,  
1567 2004.

1568 Song, M., Marcolli, C., Krieger, U., Zuend, A., and Peter, T.: Liquid-liquid phase separation in aerosol  
1569 particles: Dependence on O: C, organic functionalities, and compositional complexity,  
1570 *Geophysical research letters*, 39, 2012a.

1571 Song, M., Marcolli, C., Krieger, U., Zuend, A., and Peter, T.: Liquid-liquid phase separation and  
1572 morphology of internally mixed dicarboxylic acids/ammonium sulfate/water particles,  
1573 *Atmospheric Chemistry and Physics*, 12, 2691-2712, 2012b.

1574 Song, M., Marcolli, C., Krieger, U. K., Lienhard, D. M., and Peter, T.: Morphologies of mixed  
1575 organic/inorganic/aqueous aerosol droplets, *Faraday discussions*, 165, 289-316, 2013.

1576 Song, M., Ham, S., Andrews, R. J., You, Y., and Bertram, A. K.: Liquid–liquid phase separation in organic  
1577 particles containing one and two organic species: importance of the average O: C, *Atmospheric*  
1578 *Chemistry and Physics*, 18, 12075-12084, 2018.

1579 Steer, B., Gorbunov, B., Price, M. C., and Podoleanu, A.: Raman spectroscopic identification of size-  
1580 selected airborne particles for quantitative exposure assessment, *Measurement Science and*  
1581 *Technology*, 27, 045801, 2016.

1582 Stewart, D. J., Cai, C., Naylor, J., Preston, T. C., Reid, J. P., Krieger, U. K., Marcolli, C., and Zhang, Y.  
1583 H.: Liquid–Liquid Phase Separation in Mixed Organic/Inorganic Single Aqueous Aerosol  
1584 Droplets, *The Journal of Physical Chemistry A*, 119, 4177-4190, [10.1021/acs.jpca.5b01658](https://doi.org/10.1021/acs.jpca.5b01658),  
1585 2015.

1586 Su, H., Cheng, Y., and Pöschl, U.: New Multiphase Chemical Processes Influencing Atmospheric  
1587 Aerosols, Air Quality, and Climate in the Anthropocene, *Accounts of Chemical Research*, 53,  
1588 2034-2043, [10.1021/acs.accounts.0c00246](https://doi.org/10.1021/acs.accounts.0c00246), 2020.

1589 Sullivan, R. C., Boyer-Chelmo, H., Gorkowski, K., and Beydoun, H.: Aerosol Optical Tweezers  
1590 Elucidate the Chemistry, Acidity, Phase Separations, and Morphology of Atmospheric  
1591 Microdroplets, *Accounts of Chemical Research*, 53, 2498-2509, [10.1021/acs.accounts.0c00407](https://doi.org/10.1021/acs.accounts.0c00407),  
1592 2020.

1593 Sun, Z., Duan, F., He, K., Du, J., Yang, L., Li, H., Ma, T., and Yang, S.: Physicochemical analysis of  
1594 individual atmospheric fine particles based on effective surface-enhanced Raman spectroscopy,  
1595 *Journal of Environmental Sciences*, 75, 388-395, <https://doi.org/10.1016/j.jes.2018.06.006>,

1596 2019a.

1597 Sun, Z., Duan, F., He, K., Du, J., and Zhu, L.: Sulfate–nitrate–ammonium as double salts in PM2.5:  
 1598 Direct observations and implications for haze events, *Science of The Total Environment*, 647,  
 1599 204-209, <https://doi.org/10.1016/j.scitotenv.2018.07.107>, 2019b.

1600 Tahir, M. A., Zhang, X., Cheng, H., Xu, D., Feng, Y., Sui, G., Fu, H., Valev, V. K., Zhang, L., and Chen,  
 1601 J.: Klarite as a label-free SERS-based assay: a promising approach for atmospheric bioaerosol  
 1602 detection, *Analyst*, 145, 277-285, 10.1039/C9AN01715A, 2020.

1603 Talari, A. C. S., Movasaghi, Z., Rehman, S., and Rehman, I. U.: Raman spectroscopy of biological tissues,  
 1604 *Applied spectroscopy reviews*, 50, 46-111, 2015.

1605 Tang, M., Chan, C. K., Li, Y. J., Su, H., Ma, Q., Wu, Z., Zhang, G., Wang, Z., Ge, M., Hu, M., He, H.,  
 1606 and Wang, X.: A review of experimental techniques for aerosol hygroscopicity studies, *Atmos.*  
 1607 *Chem. Phys.*, 19, 12631-12686, 10.5194/acp-19-12631-2019, 2019.

1608 Tang, M. J., Camp, J. C. J., Rkiouak, L., McGregor, J., Watson, I. M., Cox, R. A., Kalberer, M., Ward, A.  
 1609 D., and Pope, F. D.: Heterogeneous Interaction of SiO<sub>2</sub> with N<sub>2</sub>O<sub>5</sub>: Aerosol Flow Tube and  
 1610 Single Particle Optical Levitation–Raman Spectroscopy Studies, *The Journal of Physical*  
 1611 *Chemistry A*, 118, 8817-8827, 10.1021/jp506753c, 2014.

1612 Tirella, P. N., Craig, R. L., Tubbs, D. B., Olson, N. E., Lei, Z., and Ault, A. P.: Extending surface enhanced  
 1613 Raman spectroscopy (SERS) of atmospheric aerosol particles to the accumulation mode (150–  
 1614 800 nm), *Environmental Science: Processes & Impacts*, 20, 1570-1580, 10.1039/C8EM00276B,  
 1615 2018.

1616 Tobon, Y. A., Seng, S., Picone, L. A., Bava, Y. B., Juncal, L. C., Moreau, M., Romano, R. M., Barbillat,  
 1617 J., and Sobanska, S.: Photochemistry of single particles using acoustic levitation coupled with  
 1618 Raman microspectrometry, *Journal of Raman Spectroscopy*, 48, 1135-1137,  
 1619 <https://doi.org/10.1002/jrs.5181>, 2017.

1620 Tobon, Y. A., El Hajj, D., Seng, S., Bengrad, F., Moreau, M., Visez, N., Chiapello, I., Crumeyrolle, S.,  
 1621 and Choël, M.: Impact of the particle mixing state on the hygroscopicity of internally mixed  
 1622 sodium chloride–ammonium sulfate single droplets: a theoretical and experimental study,  
 1623 *Physical Chemistry Chemical Physics*, 23, 14391-14403, 2021.

1624 Tolles, W. M., Nibler, J., McDonald, J., and Harvey, A.: A review of the theory and application of  
 1625 coherent anti-Stokes Raman spectroscopy (CARS), *Applied Spectroscopy*, 31, 253-271, 1977.

1626 Treuel, L., Pederzani, S., and Zellner, R.: Deliquescence behaviour and crystallisation of ternary  
 1627 ammonium sulfate/dicarboxylic acid/water aerosols, *Physical Chemistry Chemical Physics*, 11,  
 1628 7976-7984, 10.1039/B905007H, 2009.

1629 Tripathi, A., Jabbour, R. E., Guicheteau, J. A., Christesen, S. D., Emge, D. K., Fountain, A. W., Bottiger,  
 1630 J. R., Emmons, E. D., and Snyder, A. P.: Bioaerosol Analysis with Raman Chemical Imaging  
 1631 Microspectroscopy, *Analytical Chemistry*, 81, 6981-6990, 10.1021/ac901074c, 2009.

1632 Tsai, J.-H. M., Harrison, J. G., Martin, J. C., Hamilton, T. P., van der Woerd, M., Jablonsky, M. J., and  
 1633 Beckman, J. S.: Role of Conformation of Peroxynitrite Anion (ONOO<sup>-</sup>) with Its Stability and  
 1634 Toxicity, *Journal of the American Chemical Society*, 116, 4115-4116, 10.1021/ja00088a072,  
 1635 1994.

1636 Uraoka, M., Maegawa, K., and Ishizaka, S.: Raman Spectroscopy of Single Light-Absorbing  
 1637 Carbonaceous Particles Levitated in Air Using an Annular Laser Beam, *Analytical Chemistry*,  
 1638 89, 12866-12871, 10.1021/acs.analchem.7b03455, 2017.

1639 Vejpongsa, I., Suvachittanont, S., Klinklan, N., Thongyen, T., Veres, M., and Szymanski, W. W.:

1640 Deliberation between PM1 and PM2.5 as air quality indicators based on comprehensive  
1641 characterization of urban aerosols in Bangkok, Thailand, *Particuology*, 35, 1-9,  
1642 <https://doi.org/10.1016/j.partic.2017.05.001>, 2017.

1643 Wang, C., Pan, Y.-L., Hill, S. C., and Redding, B.: Photophoretic trapping-Raman spectroscopy for single  
1644 pollens and fungal spores trapped in air, *Journal of Quantitative Spectroscopy and Radiative*  
1645 *Transfer*, 153, 4-12, 2015a.

1646 Wang, M., Zheng, N., Zhao, D., Shang, J., and Zhu, T.: Using Micro-Raman Spectroscopy to Investigate  
1647 Chemical Composition, Mixing States, and Heterogeneous Reactions of Individual  
1648 Atmospheric Particles, *Environmental Science & Technology*, 55, 10243-10254,  
1649 [10.1021/acs.est.1c01242](https://doi.org/10.1021/acs.est.1c01242), 2021a.

1650 Wang, W., Lei, T., Zuend, A., Su, H., Cheng, Y., Shi, Y., Ge, M., and Liu, M.: Effect of mixing structure  
1651 on the water uptake of mixtures of ammonium sulfate and phthalic acid particles, *Atmospheric*  
1652 *Chemistry and Physics*, 21, 2179-2190, 2021b.

1653 Wang, X., Jing, B., Tan, F., Ma, J., Zhang, Y., and Ge, M.: Hygroscopic behavior and chemical  
1654 composition evolution of internally mixed aerosols composed of oxalic acid and ammonium  
1655 sulfate, *Atmos. Chem. Phys.*, 17, 12797-12812, [10.5194/acp-17-12797-2017](https://doi.org/10.5194/acp-17-12797-2017), 2017.

1656 Wang, Y., Ma, J.-B., Zhou, Q., Pang, S.-F., and Zhang, Y.-H.: Hygroscopicity of Mixed  
1657 Glycerol/Mg(NO<sub>3</sub>)<sub>2</sub>/Water Droplets Affected by the Interaction between Magnesium Ions and  
1658 Glycerol Molecules, *The Journal of Physical Chemistry B*, 119, 5558-5566,  
1659 [10.1021/acs.jpcc.5b00458](https://doi.org/10.1021/acs.jpcc.5b00458), 2015b.

1660 Wei, H., Vejerano, E. P., Leng, W., Huang, Q., Willner, M. R., Marr, L. C., and Vikesland, P. J.: Aerosol  
1661 microdroplets exhibit a stable pH gradient, *Proceedings of the National Academy of Sciences*,  
1662 115, 7272-7277, [10.1073/pnas.1720488115](https://doi.org/10.1073/pnas.1720488115), 2018.

1663 Wheeler, M. J., Mason, R. H., Steunenberg, K., Wagstaff, M., Chou, C., and Bertram, A. K.: Immersion  
1664 Freezing of Supermicron Mineral Dust Particles: Freezing Results, Testing Different Schemes  
1665 for Describing Ice Nucleation, and Ice Nucleation Active Site Densities, *The Journal of Physical*  
1666 *Chemistry A*, 119, 4358-4372, [10.1021/jp507875q](https://doi.org/10.1021/jp507875q), 2015.

1667 Willis, M. D., Rovelli, G., and Wilson, K. R.: Combining Mass Spectrometry of Picoliter Samples with  
1668 a Multicompartment Electrodynamic Trap for Probing the Chemistry of Droplet Arrays,  
1669 *Analytical Chemistry*, 92, 11943-11952, [10.1021/acs.analchem.0c02343](https://doi.org/10.1021/acs.analchem.0c02343), 2020.

1670 Wise, M. E., Baustian, K. J., and Tolbert, M. A.: Internally mixed sulfate and organic particles as potential  
1671 ice nuclei in the tropical tropopause region, *Proceedings of the National Academy of Sciences*,  
1672 107, 6693-6698, 2010.

1673 Wise, M. E., Baustian, K. J., Koop, T., Freedman, M. A., Jensen, E. J., and Tolbert, M. A.: Depositional  
1674 ice nucleation onto crystalline hydrated NaCl particles: a new mechanism for ice formation in  
1675 the troposphere, *Atmospheric Chemistry and Physics*, 12, 1121-1134, 2012.

1676 Wu, F.-M., Wang, X.-W., Jing, B., Zhang, Y.-H., and Ge, M.-F.: Liquid-liquid phase separation in  
1677 internally mixed magnesium sulfate/glutaric acid particles, *Atmospheric Environment*, 178,  
1678 286-292, <https://doi.org/10.1016/j.atmosenv.2018.02.012>, 2018a.

1679 Wu, H. B., Chan, M. N., and Chan, C. K.: FTIR Characterization of Polymorphic Transformation of  
1680 Ammonium Nitrate, *Aerosol Science and Technology*, 41, 581-588,  
1681 [10.1080/02786820701272038](https://doi.org/10.1080/02786820701272038), 2007.

1682 Wu, H. B., and Chan, C. K.: Effects of potassium nitrate on the solid phase transitions of ammonium  
1683 nitrate particles, *Atmospheric Environment*, 42, 313-322, 2008.



1684 Wu, L., Becote, C., Sobanska, S., Flaud, P. M., Perraudin, E., Villenave, E., Song, Y. C., and Ro, C. U.:  
1685 Hygroscopic behavior of aerosols generated from solutions of 3-methyl-1,2,3-  
1686 butanetricarboxylic acid, its sodium salts, and its mixtures with NaCl, *Atmos. Chem. Phys.*, 20,  
1687 14103-14122, 10.5194/acp-20-14103-2020, 2020.

1688 Wu, Z., Wang, Y., Tan, T., Zhu, Y., Li, M., Shang, D., Wang, H., Lu, K., Guo, S., Zeng, L., and Zhang,  
1689 Y.: Aerosol Liquid Water Driven by Anthropogenic Inorganic Salts: Implying Its Key Role in  
1690 Haze Formation over the North China Plain, *Environmental Science & Technology Letters*, 5,  
1691 160-166, 10.1021/acs.estlett.8b00021, 2018b.

1692 Xu, G., Cheng, H., Jones, R., Feng, Y., Gong, K., Li, K., Fang, X., Tahir, M. A., Valev, V. K., and Zhang,  
1693 L.: Surface-Enhanced Raman Spectroscopy Facilitates the Detection of Microplastics <1  $\mu\text{m}$  in  
1694 the Environment, *Environmental Science & Technology*, 54, 15594-15603,  
1695 10.1021/acs.est.0c02317, 2020a.

1696 Xu, R., Ge, Y., Kwong, K. C., Poon, H. Y., Wilson, K. R., Yu, J. Z., and Chan, M. N.: Inorganic Sulfur  
1697 Species Formed upon Heterogeneous OH Oxidation of Organosulfates: A Case Study of Methyl  
1698 Sulfate, *ACS Earth and Space Chemistry*, 4, 2041-2049, 10.1021/acsearthspacechem.0c00209,  
1699 2020b.

1700 Ye, J., Abbatt, J. P. D., and Chan, A. W. H.: Novel pathway of SO<sub>2</sub> oxidation in the atmosphere: reactions  
1701 with monoterpene ozonolysis intermediates and secondary organic aerosol, *Atmos. Chem. Phys.*,  
1702 18, 5549-5565, 10.5194/acp-18-5549-2018, 2018.

1703 Yeung, M. C., and Chan, C. K.: Water Content and Phase Transitions in Particles of Inorganic and  
1704 Organic Species and their Mixtures Using Micro-Raman Spectroscopy, *Aerosol Science and  
1705 Technology*, 44, 269-280, 10.1080/02786820903583786, 2010.

1706 Yeung, M. C., Ling, T. Y., and Chan, C. K.: Effects of the Polymorphic Transformation of Glutaric Acid  
1707 Particles on Their Deliquescence and Hygroscopic Properties, *The Journal of Physical  
1708 Chemistry A*, 114, 898-903, 10.1021/jp908250v, 2010.

1709 You, Y., Renbaum-Wolff, L., Carreras-Sospedra, M., Hanna, S. J., Hiranuma, N., Kamal, S., Smith, M.  
1710 L., Zhang, X., Weber, R. J., Shilling, J. E., Dabdub, D., Martin, S. T., and Bertram, A. K.: Images  
1711 reveal that atmospheric particles can undergo liquid-liquid phase separations, *Proceedings of  
1712 the National Academy of Sciences*, 109, 13188, 10.1073/pnas.1206414109, 2012.

1713 Yu, J.-Y., Zhang, Y., Tan, S.-H., Liu, Y., and Zhang, Y.-H.: Observation on the Ion Association Equilibria  
1714 in NaNO<sub>3</sub> Droplets Using Micro-Raman Spectroscopy, *The Journal of Physical Chemistry B*,  
1715 116, 12581-12589, 10.1021/jp306367v, 2012.

1716 Yu, T., Zhao, D., Song, X., and Zhu, T.: NO<sub>2</sub>-initiated multiphase oxidation of SO<sub>2</sub> by O<sub>2</sub> on CaCO<sub>3</sub>  
1717 particles, *Atmos. Chem. Phys.*, 18, 6679-6689, 2018.

1718 Zangmeister, C. D., and Pemberton, J. E.: Raman Spectroscopy of the Reaction of Sodium Chloride with  
1719 Nitric Acid: Sodium Nitrate Growth and Effect of Water Exposure, *The Journal of Physical  
1720 Chemistry A*, 105, 3788-3795, 10.1021/jp003374n, 2001.

1721 Zardini, A. A., Sjogren, S., Marcolli, C., Krieger, U. K., Gysel, M., Weingartner, E., Baltensperger, U.,  
1722 and Peter, T.: A combined particle trap/HTDMA hygroscopicity study of mixed  
1723 inorganic/organic aerosol particles, *Atmos. Chem. Phys.*, 8, 5589-5601, 10.5194/acp-8-5589-  
1724 2008, 2008.

1725 Zhang, C., Ma, N., Fan, F., Yang, Y., Größ, J., Yan, J., Bu, L., Wang, Y., and Wiedensohler, A.:  
1726 Hygroscopic growth of aerosol particles consisted of oxalic acid and its internal mixture with  
1727 ammonium sulfate for the relative humidity ranging from 80% to 99.5%, *Atmospheric*

1728 Environment, 252, 118318, 2021a.

1729 Zhang, R., Wang, G., Guo, S., Zamora, M. L., Ying, Q., Lin, Y., Wang, W., Hu, M., and Wang, Y.:  
1730 Formation of urban fine particulate matter, *Chemical reviews*, 115, 3803-3855, 2015.

1731 Zhang, R., Gen, M., Huang, D., Li, Y., and Chan, C. K.: Enhanced Sulfate Production by Nitrate  
1732 Photolysis in the Presence of Halide Ions in Atmospheric Particles, *Environmental Science &  
1733 Technology*, 54, 3831-3839, 10.1021/acs.est.9b06445, 2020a.

1734 Zhang, R., Gen, M., Fu, T.-M., and Chan, C. K.: Production of Formate via Oxidation of Glyoxal  
1735 Promoted by Particulate Nitrate Photolysis, *Environmental Science & Technology*,  
1736 10.1021/acs.est.0c08199, 2021b.

1737 Zhang, Y., Bao, F., Li, M., Xia, H., Huang, D., Chen, C., and Zhao, J.: Photoinduced Uptake and  
1738 Oxidation of SO<sub>2</sub> on Beijing Urban PM<sub>2.5</sub>, *Environmental Science & Technology*, 54, 14868-  
1739 14876, 10.1021/acs.est.0c01532, 2020b.

1740 Zhang, Y.-H., and Chan, C. K.: Study of Contact Ion Pairs of Supersaturated Magnesium Sulfate  
1741 Solutions Using Raman Scattering of Levitated Single Droplets, *The Journal of Physical  
1742 Chemistry A*, 104, 9191-9196, 10.1021/jp0013659, 2000.

1743 Zhang, Y.-H., and Chan, C. K.: Observations of Water Monomers in Supersaturated NaClO<sub>4</sub>, LiClO<sub>4</sub>,  
1744 and Mg(ClO<sub>4</sub>)<sub>2</sub> Droplets Using Raman Spectroscopy, *The Journal of Physical Chemistry A*,  
1745 107, 5956-5962, 10.1021/jp0271256, 2003.

1746 Zhang, Y.-H., Choi, M. Y., and Chan, C. K.: Relating Hygroscopic Properties of Magnesium Nitrate to  
1747 the Formation of Contact Ion Pairs, *The Journal of Physical Chemistry A*, 108, 1712-1718,  
1748 10.1021/jp036524d, 2004.

1749 Zhao, D., Song, X., Zhu, T., Zhang, Z., Liu, Y., and Shang, J.: Multiphase oxidation of SO<sub>2</sub> by NO<sub>2</sub> on  
1750 CaCO<sub>3</sub> particles, *Atmospheric Chemistry and Physics*, 18, 2481-2493, 10.5194/acp-18-2481-  
1751 2018, 2018.

1752 Zheng, G., Su, H., Wang, S., Andreae, M. O., Pöschl, U., and Cheng, Y.: Multiphase buffer theory  
1753 explains contrasts in atmospheric aerosol acidity, *Science*, 369, 1374-1377, 2020a.

1754 Zheng, H., Song, S., Sarwar, G., Gen, M., Wang, S., Ding, D., Chang, X., Zhang, S., Xing, J., and Sun,  
1755 Y.: Contribution of Particulate Nitrate Photolysis to Heterogeneous Sulfate Formation for  
1756 Winter Haze in China, *Environmental Science & Technology Letters*, 7, 632-638, 2020b.

1757 Zheng, L., Kulkarni, P., Birch, M. E., Ashley, K., and Wei, S.: Analysis of Crystalline Silica Aerosol  
1758 Using Portable Raman Spectrometry: Feasibility of Near Real-Time Measurement, *Analytical  
1759 Chemistry*, 90, 6229-6239, 10.1021/acs.analchem.8b00830, 2018.

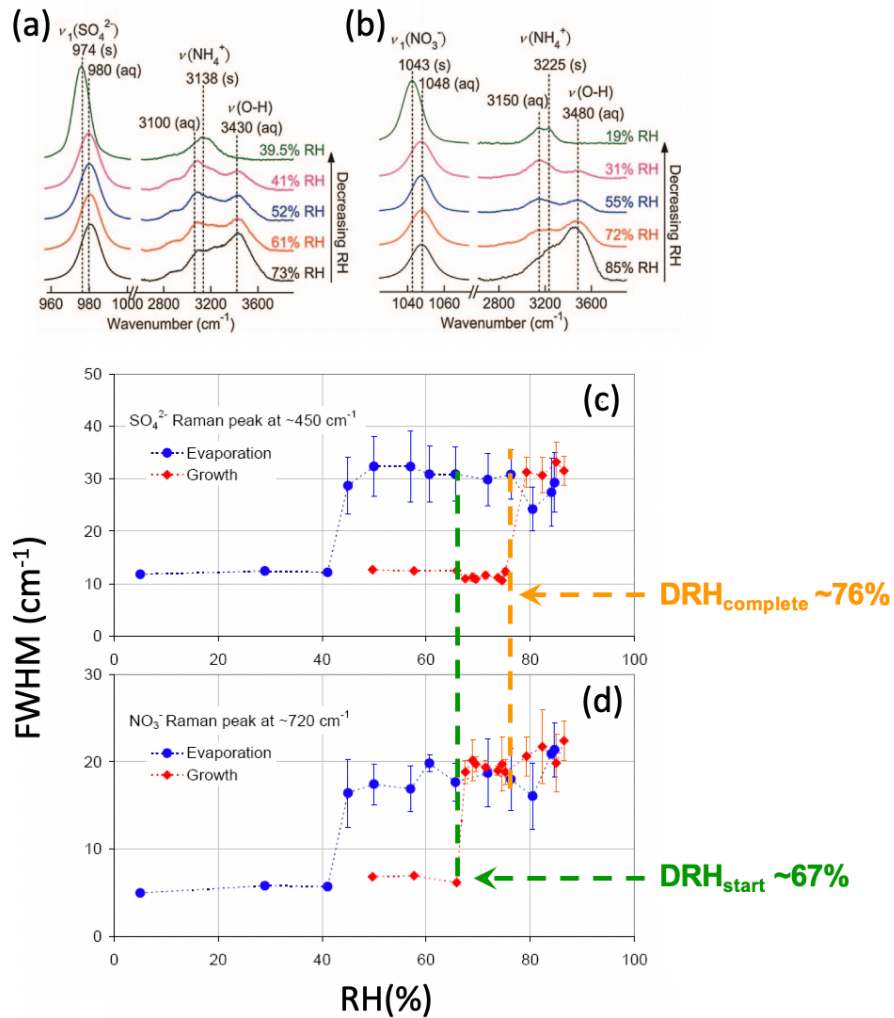
1760 Zhou, H., Yang, D., Ivleva, N. P., Mircescu, N. E., Niessner, R., and Haisch, C.: SERS Detection of  
1761 Bacteria in Water by in Situ Coating with Ag Nanoparticles, *Analytical Chemistry*, 86, 1525-  
1762 1533, 10.1021/ac402935p, 2014a.

1763 Zhou, H., Yang, D., Ivleva, N. P., Mircescu, N. E., Schubert, S., Niessner, R., Wieser, A., and Haisch, C.:  
1764 Label-Free in Situ Discrimination of Live and Dead Bacteria by Surface-Enhanced Raman  
1765 Scattering, *Analytical Chemistry*, 87, 6553-6561, 10.1021/acs.analchem.5b01271, 2015.

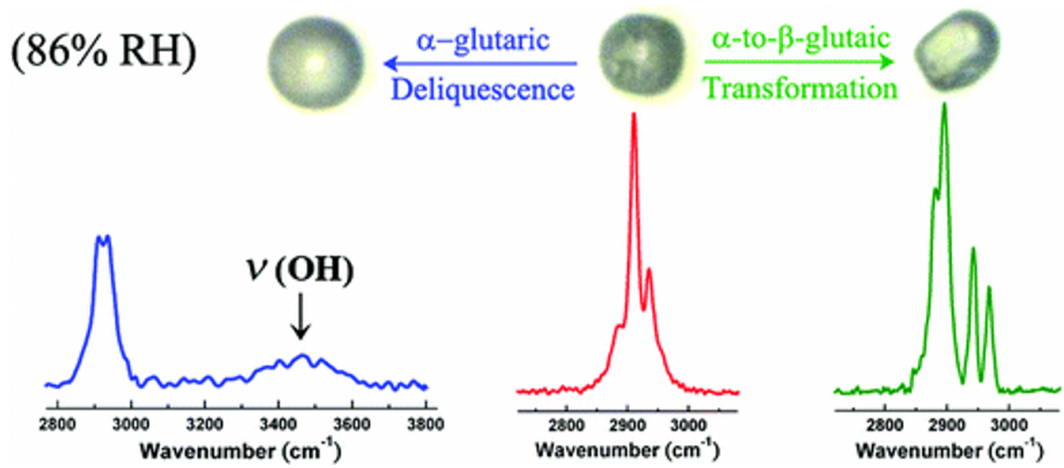
1766 Zhou, Q., Pang, S.-F., Wang, Y., Ma, J.-B., and Zhang, Y.-H.: Confocal Raman studies of the evolution  
1767 of the physical state of mixed phthalic acid/ammonium sulfate aerosol droplets and the effect  
1768 of substrates, *The Journal of Physical Chemistry B*, 118, 6198-6205, 2014b.

1769 Zhu, F., Zhou, H., Wang, X., Zhou, Y., Liu, H., Fang, C., and Fang, Y.: Raman spectroscopy and ab initio  
1770 quantum chemical calculations of ion association behavior in calcium nitrate solution, *Journal  
1771 of Raman Spectroscopy*, 49, 852-861, <https://doi.org/10.1002/jrs.5349>, 2018.

1772 Zobrist, B., Soonsin, V., Luo, B. P., Krieger, U. K., Marcolli, C., Peter, T., and Koop, T.: Ultra-slow water  
 1773 diffusion in aqueous sucrose glasses, *Physical Chemistry Chemical Physics*, 13, 3514-3526,  
 1774 2011.  
 1775



1776  
 1777 **Figure 1.** Raman spectra of a single (a) AS and (b) AN particle upon evaporation (Yeung and Chan,  
 1778 2010). FWHM of (c)  $\text{SO}_4^{2-}$  peak and (d)  $\text{NO}_3^-$  peak during the evaporation-growth cycle of a mixed AS-  
 1779 AN particle.  
 1780

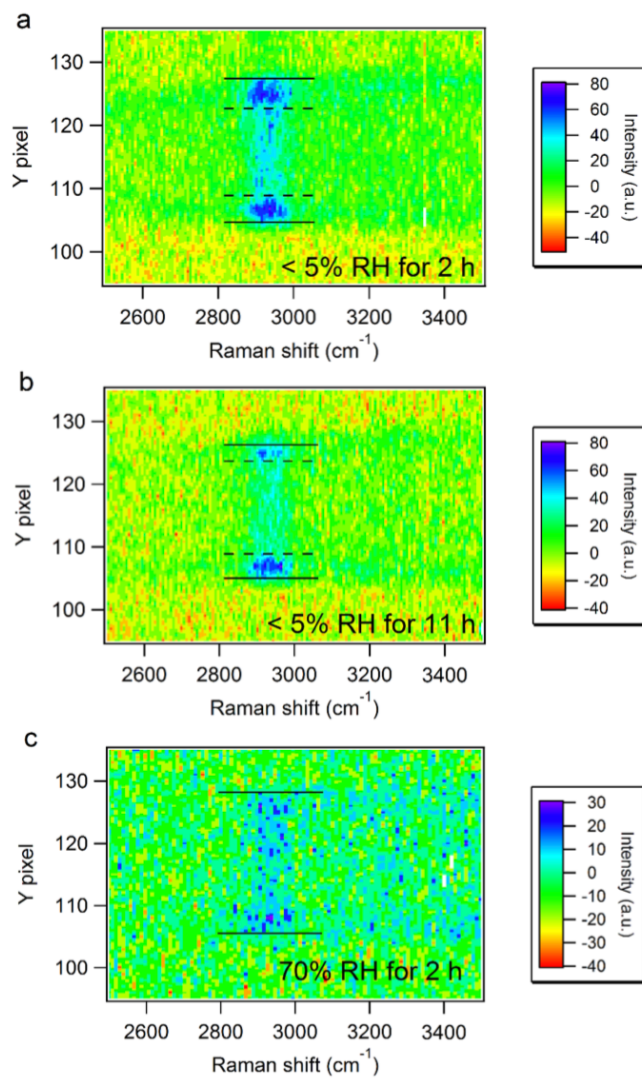


1781

1782 **Figure 2.** Raman spectra of deliquescent  $\alpha$ -glutaric acid, crystalline  $\alpha$ -glutaric acid and  $\beta$ -glutaric acid

1783 (Ling and Chan, 2007).

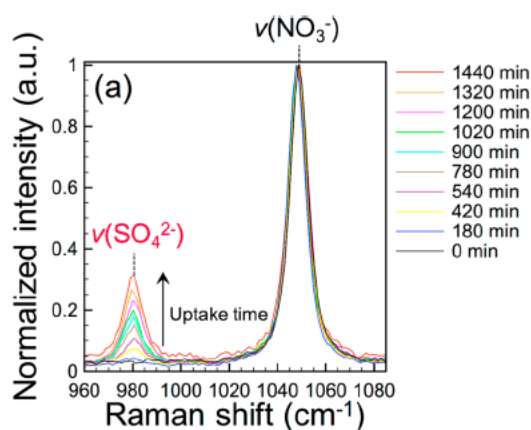
1784



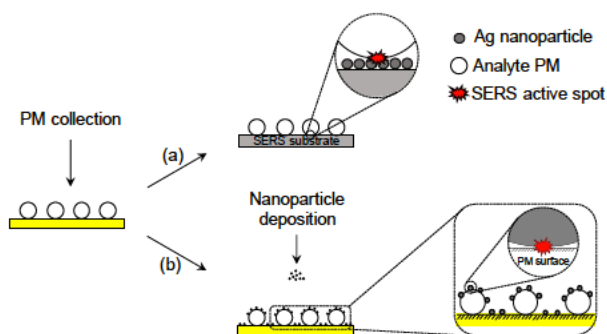
1785

1786 **Figure 3.** Spatially resolved Raman intensities of AS – sucrose (molar fraction of sucrose in total solute

1787 ( $F_{\text{SU}} = 0.5$ ) particles equilibrated (a) at < 5% RH for 2 hours and (b) for 11 h and (c) at 70% RH for 2  
 1788 hours. C-H peaks at  $\sim 2900 \text{ cm}^{-1}$  represent sucrose. Solid lines indicate the particle's upper and lower  
 1789 edges. The outer regions between the dashed and solid lines are sucrose-rich in (a)-(b) (Chu and Chan,  
 1790 2017a).  
 1791



1792  
 1793 **Figure 4.** Sulfate formation during the photolysis of AN particles in the presence of  $\text{SO}_2$  at 80% RH (Gen  
 1794 et al., 2019b).  
 1795



1796  
 1797 **Figure 5.** Schematic illustration of (a) a conventional SERS substrate approach and (b) the ES-SERS  
 1798 approach (Gen and Chan, 2017).  
 1799

1800 Appendix A. Major Raman peaks of atmospheric relevant species

Species		Raman shift ( $\text{cm}^{-1}$ )	Ref.
Water	O-H	$\sim 3300$ (monomers)	(Carey and Korenowski, 1998)
		$\sim 3600$ (hydrogen-bonded)	

Inorganic	NH <sub>4</sub> <sup>+</sup>	~1413; ~1660; ~3100	(Chu and Chan, 2017a; Sauerwein and Chan, 2017)
	SO <sub>4</sub> <sup>2-</sup>	~450; ~618; ~980	(Ling and Chan, 2007; Chu and Chan, 2017a)
	HSO <sub>4</sub> <sup>-</sup>	~1053	(Rindelaub et al., 2016; Craig et al., 2017; Craig et al., 2018)
	NO <sub>3</sub> <sup>-</sup>	~717; ~1046; ~1413	(Tobon et al., 2017; Gen et al., 2019b)
	HNO <sub>3</sub>	~1306	(Rindelaub et al., 2016)
	NO <sub>2</sub> <sup>-</sup>	~815; ~1278; ~1330	(Tobon et al., 2017)
	ONOO <sup>-</sup>	~980	(Tsai et al., 1994; Tobon et al., 2017)
	CO <sub>3</sub> <sup>2-</sup>	~1067	(Rindelaub et al., 2016)
	HCO <sub>3</sub> <sup>-</sup>	~1019	(Rindelaub et al., 2016)
Soot	D	~1367	(Ivleva et al., 2007b; Gen and Chan, 2017)
	G	~1585	(Ivleva et al., 2007b; Gen and

				Chan, 2017)	
Mineral dust	SiO <sub>2</sub>	Si-O-Si	~390; ~490; ~795; ~972; ~1460		(Laskina et al., 2013;Rkiouak et al., 2014)
		O-Si-O	~356		
		Si-O	~465		
	$\alpha$ -Al <sub>2</sub> O <sub>3</sub>	Al-O-Al	~420; ~585; ~796;		(Rkiouak et al., 2014)
		Al-OH	~976		
	Kaolinite	Si-O	~397		(Laskina et al., 2013)
		Si-O-Al	~516		
		O-H	~914; 3624; 3656; 3668; 3698		
	TiO <sub>2</sub>	Ti-O	~484; ~680;	Amorphous	(Rkiouak et al., 2014;Tang et al., 2014)
			~153; ~639;	Anatase	
O-O		~250; ~317;	Amorphous		
CaCO <sub>3</sub>	CO <sub>3</sub> <sup>2-</sup>	~713; ~1087		(Laskina et al., 2013;Yu et al., 2018;Zhao et al., 2018)	
Organic	C-H		~1400; 2700-3000		(Chu and Chan, 2017a;Gen et al., 2018b)
	C-O		~1470		(Laskina et al., 2013)
	C=O		~1700		(Yeung and Chan, 2010;Yeung et al., 2010;Bondy et al., 2018)
	O-H		~1700; 3200-3400		(Yeung and Chan, 2010;Zhou et al., 2014b)

C-N-C	~890	(Chu and Chan, 2017a)
O-C-O (ring)	~770	(Gen et al., 2018b)
ring	~950	(Gen et al., 2018b)
O-O	~850	(Lee and Chan, 2007b, a)
C=C	~1600	(Lee and Chan, 2007b; Chu et al., 2019)
C=C-C=C	~1640&1655 (double peaks)	(Lee and Chan, 2007b; Chu et al., 2019)
C=C-C=O	~1690	(Lee and Chan, 2007b; Chu et al., 2019)
RO-SO <sub>3</sub>	~846	(Bondy et al., 2018)
S-O (-SO <sub>3</sub> group)	1065	(Bondy et al., 2018)

1801